Available online at www.sciencedirect.com

ScienceDirect

Geochimica et Cosmochimica Acta 249 (2019) 173–198

Geochimica et Cosmochimica Acta

www.elsevier.com/locate/gca

Organic acids and high soil CO_2 drive intense chemical weathering of Hawaiian basalts: Insights from reactive transport models

Alida Perez-Fodich [a,b,*], Louis A. Derry [a]

[a] Department of Earth and Atmospheric Science, Cornell University, Ithaca, NY 14853, USA
[b] Department of Geology, University of Chile, Santiago, Chile

Received 15 November 2018; accepted in revised form 18 January 2019; Available online 28 January 2019

Abstract

We have investigated how biota contributes to rapid chemical weathering of Hawaiian basalts using a reactive transport model and chemical data from a soil chronosequence. These Hawaiian soils have developed under a tropical forest with rainfall >200 cm/yr and exhibit extensive weathering on timescales of 10^4 years. We developed a series of multicomponent reactive transport models to examine the role of soil respiration and low molecular weight organic acids in generating these intense weathering patterns. The base model starts with a 1-m basaltic porous media reacting with a fluid of rainwater composition in equilibrium with atmospheric CO_2. Subsequent simulations incorporate soil respiration modeled as a constant flux of CO_2 at 10× atmospheric and continuous input of organic ligands – oxalate and citrate – at 10^{-4} molar. After 20 kyr of weathering, the base model shows limited elemental losses, high soil pH and is overall CO_2(acid)-limited. Soil respiration lowers soil pH to circumneutral values, leaches all Mg and Ca from the basalt and allows precipitation of Fe(III)-oxyhydroxides, while Al stays immobile as secondary clays accumulate. After adding organic ligands, soil pH is reduced to values similar to the Hawaiian soils and Si, Al and Fe are exported from the system by dissolution of secondary phases, resulting in mass depletion patterns similar to the ones observed in Hawai'i. Dissolution of secondary minerals is generated by low pH and relatively low free activities of Al^{3+} and Fe^{3+} when organic ligands are added. These results suggest that organic acids in basalt weathering in tropical environments can sustain far-from-equilibrium conditions that drive fast elemental losses and that biologic activity contributes to weathering processes both by generating high soil P_{CO2} and organic acids.

Keywords: Chemical weathering; Reactive Transport Model; Hawaii; Basalt; Chronosequence; CrunchFlow; Critical Zone

1. INTRODUCTION

Weathering of volcanic rocks in tropical environments can produce a regolith that is strongly depleted in base cations and silica over geologically short time scales. Weathering rates in such settings are rapid, whether estimated from modern stream fluxes (Louvat and Allegre, 1997; Dessert et al., 2001; Schopka et al., 2011; Schopka and Derry, 2012; Li et al., 2016) or from studies of pedogenesis (Stewart et al., 1998; Hedin et al., 2003). Base cation depletion, significant Si losses, Al and Fe mobilization and low soil pH are common characteristics in these types of landscapes (Vitousek et al., 1997; Chadwick et al., 1999; Nieuwenhuyse et al., 2000; Zehetner et al., 2003; He et al., 2008). Rapid rock weathering and fast pedogenesis result from a combination of kinetic and thermodynamic factors enhancing weathering rates. Mineral solubility, precipitation of secondary phases, fluid residence time, reactive gases – CO_2 and O_2 – and input of reactive organic compounds from root leachates and exudates from microbial

* Corresponding author at: Department of Earth and Atmospheric Science, Cornell University, Ithaca, NY 14853, USA.
E-mail address: ap868@cornell.edu (A. Perez-Fodich).

https://doi.org/10.1016/j.gca.2019.01.027
0016-7037/

and mycorrhizal fungi are some of the variables that have been identified to contribute to intense weathering. However, their interactions and individual controls in weathering of volcanic rocks in tropical settings are usually hard to unravel. Understanding the mechanisms that drive fast weathering is important in modern and ancient natural systems because chemical weathering is a key component of global biogeochemical cycles. Chemical weathering controls elemental fluxes from the land to rivers and oceans (Bluth and Kump, 1994; Louvat and Allegre, 1997; Viers et al., 2009; Schopka et al., 2011; Dessert et al., 2015), delivers nutrients to ecosystems (Chadwick et al., 1999; Buss et al., 2010; Wymore et al., 2017), and ultimately, consumes atmospheric CO_2 regulating climate over geological timescales (Walker et al., 1981; Berner et al., 1983; Berner, 1992; Gaillardet et al., 1999; Kump et al., 2000).

The role of plants and microbiological activity has been suggested as an important agent enhancing mineral weathering by several authors (Schwartzman and Volk, 1989; Berner, 1992; Berner and Cochran, 1998; Moulton and Berner, 1998; Moulton et al., 2000; Amundson et al., 2007; Schwartzman, 2017). There are numerous ways by which biota enhances weathering with direct influence over the reactive surface or the chemical affinity of the parent materials. Plants contribute to erosion on hillslopes, while root induced break-up creates secondary porosity structures preferential for advective fluid flow and reactive gases. Additionally, evapotranspiration contributes to sustain soil water and regulate runoff. Microbial respiration of organic matter can dramatically increase soil P_{CO2} which has a direct effect on the dissolution of silicate minerals. Low molecular weight organic acids (LMWOA) are ubiquitous in tropical soils and play an important role in mineral dissolution (Furrer and Stumm, 1986; Zinder et al., 1986; Barman et al., 1992; Jones and Darrah, 1994; Berggren and Mulder, 1995; Drever and Stillings, 1997; Jones, 1998; van Hees et al., 2000; Taylor et al., 2009; Lawrence et al., 2014). Organic acids control mineral dissolution and precipitation rates in three ways: (1) increasing proton activity which affects mineral saturation state (Barman et al., 1992; Gislason et al., 1996); (2) complexation of organic ligands with metals like Al and Fe, decreasing their free aqueous activities (Berggren and Mulder, 1995; Drever and Stillings, 1997; Oelkers and Schott, 1998) and increasing their total solubility (Neaman et al., 2005b, 2006; Li et al., 2006; Lawrence et al., 2014); and (3) ligand-promoted dissolution, which can accelerate weathering rates due to ligand adsorption on mineral surfaces (Amrhein and Suarez, 1988; Jones, 1998; Cama and Ganor, 2006; Li et al., 2006; Stillings et al., 1998; Ganor et al., 2009), but can also hinder dissolution as reactive surface sites become occupied (Johnson et al., 2004).

Investigation of the combined effects of LMWOA and P_{CO2} is necessary to further understand the mechanisms by which biota contributes to rapid weathering rates. Reactive transport models (RTMs) provide insight into the results of field and laboratory experiments and can be used to decipher and quantify individual contributions of reaction networks (Dontsova et al., 2009; Brantley and Lebedeva, 2011; Navarre-Sitchler et al., 2011; Godderis et al., 2013; Li et al., 2017). Combining RTMs with chemical data from soil chronosequences provides an advantage for investigating mineral weathering in natural systems (Maher et al., 2009; Moore et al., 2012; Lawrence et al., 2014); as they can help to quantitively assess the effect of combined chemical reactions in a spatially and temporally resolved framework. Additionally, in cases where mineralogy is poorly constrained, RTMs are a powerful tool to understand how dissolution and precipitation of modeled mineral phases influence the chemistry of reacting fluids and porous-media.

In this study we use the reactive transport modeling code CrunchFlow (Steefel et al., 2015) to investigate the factors controlling weathering of basalts in soils of different ages from a well-studied basaltic chronosequence in the Island of Hawai'i (Kitayama et al., 1995; Vitousek et al., 1997; Vitousek, 2004). A warm and wet climate and young eruptive ages create conditions conducive to rapid weathering and the soils in this study are significantly altered on a 10-kyr timescale. These basaltic soils show intense weathering patterns: (1) rapid depletion of base cations (Vitousek, 2004); (2) substantial losses of Al and Fe (Chadwick et al., 1999); (3) low soil pH (Hedin et al., 2003); and (4) predominance of non-crystalline secondary minerals including aluminosilicates such as allophane and imogolite, and iron hydroxides like ferrihydrite and nano-goethite (Chorover et al., 2004; Thompson et al., 2006). We have developed a series of simulations designed to test the impact of different drivers of weathering of young Hawaiian basalts. We compare the results of those simulations to the observed soil chemistry data. This experiment allows us to test the biological activity effects on rapid weathering rates such as soil P_{CO2} and LMWOA; plus, other parameters such as different kinetic formulations for dissolution and Fe oxidation. We hypothesize that the extreme weathering patterns observed in Hawaiian basalts are developed under persistent far-from-equilibrium conditions that result from a combination of factors mentioned above.

2. SITE DESCRIPTION AND DATA AVAILABLE

Sites of 0.3 and 20 kyrs were selected from the well characterized "Long Substrate Age Gradient" (LSAG) chronosequence in the Island of Hawai'i (Fig. 1) (Crews et al., 1995; Vitousek et al., 1997; Vitousek, 2004). Classification and nomenclature of the sites will follow previous papers and short summary of the sites characteristics and relevance will be discussed here. The LSAG sites included are: Thurston (300 yr) and Laupahoehoe (20,000 yr). We have excluded the Ola'a (2100 yr) from the original LSAG chronosequence, because it is overlain by the 0.3 kyr ash layer (similar to Thurston site) and several of the soil measurements in the Ola'a site are influenced by this younger ash layer (Vitousek, 2004). The parent material from both sites consist of basaltic tephra containing basaltic glass, olivine, clinopyroxene, plagioclase and magnetite-ilmenite (Vitousek et al., 1997). The youngest Thurston soils are derived from tholeiitic basalt, and the oldest Laupahoehoe soils are developed from alkalic basalts (Kurtz et al., 2000). Both sites are montane rainforest with dominant native

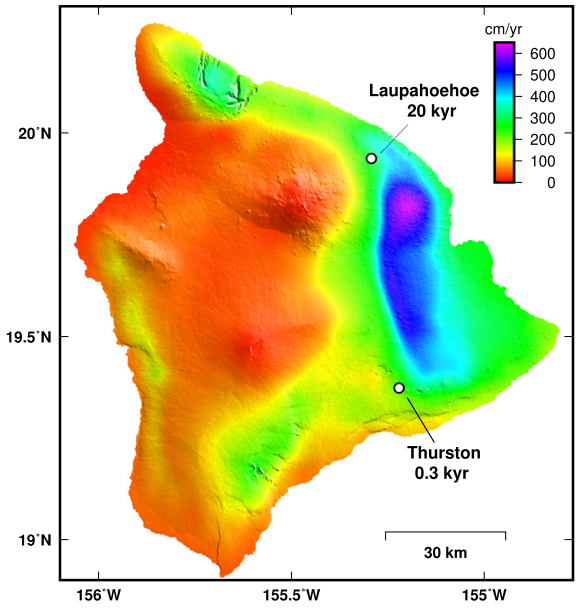

Fig. 1. Location of the two LSAG sites overlaid on a hillshade relief map of the Island of Hawai'i. The color scale represents mean annual rainfall in centimeters. Rainfall data is interpolated from raingage stations across the island by the Rainfall Atlas of Hawai'i project (Giambelluca et al., 2013). Elevation data is from the SRTM30 DEM (Becker et al., 2009). The map was generated using Generic Mapping Tools (Wessel et al., 2013). (For interpretation of the color legend, the reader is referred to the online version of this article).

species *Metrosideros polymorpha*, mean annual precipitation in all sites is circa 250 cm/yr (Giambelluca et al., 2013) and evapotranspiration in the montane rainforest is ca. 50% of MAP (Engott, 2011). Mean annual temperature is 16 °C. Finally, these sites have experienced negligible erosion and are located on constructional volcanic surfaces. Bulk and trace elemental chemistry, and soil mineralogy of the LSAG sites have been extensively described by many authors (Crews et al., 1995; Vitousek et al., 1997; Chadwick et al., 1999; Kurtz et al., 2000; Kurtz et al., 2001; Vitousek et al., 2001; Chadwick et al., 2003; Chorover et al., 2004; Vitousek, 2004). In summary, the LSAG soils are progressively depleted in Si and base cation and show a clear evidence of Al and Fe mobility and loss from the parent material within 20 kyr. In addition, soil pH is low and reaches values below 4.5.

3. METHODS: REACTIVE TRANSPORT MODELING

In this study we have set up a series of 1D-simulations based on a 1-meter long basaltic porous media column reacting with a fluid of rainwater composition in regime dominated by advective transport. We sequentially incorporate the following weathering drivers to our model: (1) Flow and reaction under varying soil water saturation conditions; (2) variations in soil CO_2 fugacity; and (3) low molecular weight organic acids (LMWOA) allowing complexation of aqueous Al and Fe(III). Calculations were carried out up to 20 kyrs, and the modeled soil solid phase chemistry compared to measured values at 0.3 and 20 kyrs (Table 1).

3.1. Model parameters

3.1.1. Mineralogy and thermodynamic properties

A simplified basaltic mineralogy is used to describe the solid domain in the system to represent the mineral assemblage of a Hawaiian basaltic tephra (Macdonald et al., 1984) consisting of calcic plagioclase, augite pyroxene, olivine, basaltic glass and magnetite which accounts for initial ferric Fe in the basalts (see abundances in Table 2). Secondary minerals allowed to precipitate include two amorphous aluminosilicates allophane and imogolite, plus goethite. The occurrence of these minerals has been widely documented to be product of early stages of basalt weathering, characteristic of young Hawaiian soils and representative of their low pH conditions (Vitousek et al., 1997; Chadwick et al., 1999; Chorover et al., 2004; Thompson et al., 2006). Further processes involving the transformation of these amorphous, early-forming phases to crystalline minerals such as smectite, hematite, kaolinite and gibbsite are outside of the scope and time frame of this study. Solubility constants for all reacting minerals are reported in Table 2.

We have attempted to maintain internal consistency between the selected mineral phases and the thermodynamic database used in our set of simulations. The abundance of thermodynamic data compilations makes this task difficult, because in most cases it is hard to determine the original data sources (Oelkers et al., 2009; Wolery and Colon, 2017). The core database used here is the LLNL database (Delany and Wolery, 1989; Wolery, 1992), which consists of equilibrium constants for aqueous, gas and mineral species mostly originating from the SUPCRT92 package and further updates (Johnson et al., 1992; Zimmer et al., 2016). While the SUPCRT92 database is not a source itself, it is based on the regression of commonly used datasets generated by several authors (Helgeson et al., 1978; Shock and Helgeson, 1988; Shock and Koretsky, 1993; Pokrovskii and Helgeson, 1995, 1997; Shock et al., 1997; Sverjensky et al., 1997). Following the approach by Aradottir et al. (2012b), instead of using solid solution end-members, we added to this dataset binary and quaternary solid solutions for olivine $Fo_{80}Fa_{20}$ and augite pyroxene $Di_{45}Hd_{25}En_{19}Fs_{11}$. Solubility for olivine and augite pyroxene were obtained by Stefansson (2001) and the calculation of equilibrium constants by Aradottir et al. (2012b) was done using SUPCRT92. As for the feldspar phase, we used the original anorthite data in the database (Helgeson et al., 1978; Johnson et al., 1992). We chose not to use the solid-solution plagioclase by Aradottir et al. (2012b), because its calculated solubility constant is much higher than reported values for plagioclase end-members in SUPCRT92 (Helgeson et al., 1978; Johnson et al., 1992). This difference arises from their use of the low-ordered plagioclase solubility model (Stefansson, 2001), for which the entropy term is higher. The magnetite and goethite equilibrium constants we use are also from the original database (Johnson et al., 1992). Equilibrium

Table 1
Summary of the parameters changed for each simulation presented in this study. Three sensitivity tests were performed for model M1 consisting of varying degrees of water saturation at 30, 70, 100%. No sub-simulations were run for model M2. For model M3 three sensitivity tests were run to test: (1) No complexation of Al and Fe(III) with organic ligands; (2) parallel Al-inhibition dissolution rate law (results not show as no differences were found); and (3) Acid Fe oxidation rate law.

	Model M1	Model M2	Model M3
Infiltrating fluid composition	Rainfall (Table 3)	Rainfall (Table 3)	Rainfall (Table 3)
CO_2 treatment	Fluid is only in equilibrium with CO_2 at 300 ppmv	Constant flux of CO_2 from inlet at 3000 ppmv	Constant flux of CO_2 from inlet at 3000 ppmv
Organic acids	No	No	Yes
Complexation of organic ligands with Al and Fe	No	No	Yes and No
Plagioclase and basaltic glass dissolution rate law	Linear-TST	Linear-TST	Linear-TST Parallel Al-inhibition
Fe oxidation rate law	Neutral oxidation	Neutral Oxidation	Neutral Oxidation Acid Oxidation
Water saturation	30% – 50% – 70% and 100%	50%	50%
Number of sensitivity tests	3	0	3

constants for the secondary minerals allophane and imogolite were calculated by Aradottir et al. (2012b) based on Gibbs energy calculations obtained by Stefansson and Gislason (2001) using the SUPCRT92 package.

The glass composition is derived from the BHVO-2 Hawaiian basalt (Wilson, 1997). Reported Fe_2O_3 (total Fe) was stoichiometrically replaced with ferrous iron. TiO_2 and P_2O_5, which make up for 2.73 and 0.27% of the total rock composition respectively, were omitted in calculating the basaltic glass solubility since both elements are not included in the model basis. The resulting composition of the BHVO-2 glass normalized to one Si atom is: $SiAl_{.32}Fe(II)_{.09}Mg_{.22}Ca_{.24}Na_{.09}K_{.01}O_{3.08}$. Computation of the equilibrium constant (log K) for basaltic glass dissolution follows the oxide composition method proposed by Paul (1977). This approach has been widely used to determine solubilities of aluminosilicate and borosilicate glasses at formation temperatures ranging from 25 to 90 °C (Bourcier et al., 1992; Advocat et al., 1997; Leturcq et al., 1999; Techer et al., 2001; Aradottir et al., 2012b). The solubility of the glass phase is calculated using an ideal solid-solution relation:

$$\log(K_{glass}) = \sum_i x_i \log(K_i) + \sum_i x_i \log(x_i) \quad (1)$$

where x_i is the mole fraction and K_i the solubility product of the constituting oxides in the glass phase. All log K_i values and dissolution reactions used to calculate the equilibrium constant for the BHVO-2 basaltic glass at 25 °C are presented in Table B.1 and are derived from the values used in SUPCRT92. The calculated equilibrium constant for the BHVO-2 basaltic glass is similar to K_{eq} values for forsterite and comparable to solubility constants calculated for other silicate glass compositions calculated by this method (Advocat et al., 1997; Aradottir et al., 2012b; Dontsova et al., 2009).

3.1.2. Dissolution and precipitation kinetics

Mineral dissolution and precipitation kinetics follow the general equation usually referred to as the transition state theory after work by Lasaga (1981) and expanded by Aagaard and Helgeson (1982); Hellmann and Tisserand (2006) and Lasaga (1984). For this study, we used two types of TST rate law formulations. First a linear model (R_L, Eq. (2)) with no inhibitory or promoting species dependency:

$$R_L = A_{bulk} k \left[1 - \exp\left(\frac{-\Delta G_r}{RT}\right)\right] \quad (2)$$

where R is the reaction rate for a mineral (mol m^{-3} s^{-1} porous medium), A_{bulk} is the reactive surface area (m^2 m^{-3} porous medium), k is the rate constant for the reaction (mol m^{-2} s^{-1}) and ΔG_r is Gibbs free energy of the reaction. The second is an Al-inhibition model (R_{AI}, Eq. (3)) to evaluate the promoting effects of H^+ activity and inhibition by free Al^{3+} on plagioclase and basaltic glass dissolution:

$$R_{Al} = A_{bulk} k \frac{a_{H^+}^{n_1}}{a_{Al^{3+}}^{n_2}} \left[1 - \exp\left(\frac{-\Delta G_r}{RT}\right)\right] \quad (3)$$

Here, a_{H+} and a_{Al3+} are the activities of hydrogen and aluminum ions, and n_1 and n_2 are their respective power dependencies. This formulation reflects the hypothesis that dissolution rates of aluminosilicates are controlled by the formation and destruction of Al-deficient and Si-rich precursor complexes (Oelkers et al., 1994; Oelkers and Gislason, 2001; Gislason and Oelkers, 2003).

Parallel rate-law formulations for aluminosilicates were not considered for this set of simulations. TST-like rate laws can over-estimate dissolution rates near equilibrium (Oelkers et al., 1994; Hellmann and Tisserand, 2006; Maher et al., 2009; Moore et al., 2012; Gruber et al., 2013; Zhu et al., 2016), requiring a more appropriate expression capturing this slower pathway, but given the intense weathering conditions prescribed in our model, we expect that the system should stay at far-from-equilibrium conditions. Thus, we did not include parallel rate laws for dissolution in the model.

Dissolution rate constants for all minerals were chosen from published values summarized by Palandri and Kharaka (2004) (Table 2). Forsterite is the most studied olivine end-member; we used the rate constant for the Fo80Fa20 olivine solid-solution from forsterite measurements by Pokrovsky and Schott (2000). Similarly, the rate

Table 2
Description of mineral dissolution reactions and summary of initial mineral abundances, specific surface areas, dissolution equilibrium constants and rate constants used in the model formulation.

Mineral	Dissolution Reaction Stoichiometry	Vol. %	SSA ($m^2\ g^{-1}$)	log $K_{m,eq}$	log k_m (mol $m^{-2}\ s^{-1}$)
Olivine ($Fo_{80}Fa_{20}$)	$(Mg_{0.8}Fe_{0.2})_2SiO_4 + 4\ H^+ \rightarrow 1.6\ Mg^{2+} + 0.4\ Fe^{2+} + SiO_{2(aq)} + 2\ H_2O$	12	0.1	26.72[a]	−12.47[e]
Augite ($Di_{45}Hd_{25}En_{19}Fs_{11}$)	$Ca_{0.35}Mg_{0.42}Fe_{0.23}SiO_3 + 2\ H^+ \rightarrow 0.35\ Ca^{2+} + 0.42\ Mg^{2+} + 0.23\ Fe^{2+} + SiO_{2(aq)} + H_2O$	8	0.1	10.45[a]	−12.47[f]
Anorthite	$CaAl_2Si_2O_8 + 8\ H^+ \rightarrow Ca^{2+} + 2\ Al^{3+} + 2\ SiO_{2(aq)} + 4\ H_2O$	20	0.2	26.59[b]	−12.90[g]
Magnetite	$Fe(II)Fe(III)_2O_4 + 8\ H^+ \rightarrow Fe^{2+} + 2\ Fe^{3+} + 4\ H_2O$	3	0.1	10.47[b]	−9.59[h]
Basaltic Glass (BHVO-2)	$SiAl_{0.32}Fe(II)_{0.09}Mg_{0.22}Ca_{0.24}Na_{0.09}K_{0.01}O_{3.08} + 2.16\ H^+ \rightarrow SiO_{2(aq)} + 0.32\ Al^{3+} + 0.09\ Fe^{2+} + 0.22\ Mg^{2+} + 0.24\ Ca^{2+} + 0.09\ Na^+ + 0.01\ K^+ + 1.08\ H_2O$	25	1	27.35[c]	−11.65[i]
Allophane	$Al_2O_3(SiO_2)_{1.22}(H_2O)_{2.5} + 6\ H^+ \rightarrow 2\ Al^{3+} + 1.22\ SiO_{2(aq)} + 5.5\ H_2O$	-	1	10.96[d]	−9.42[j]
Imogolite	$Al_2SiO_3(OH)_4 + 6\ H^+ \rightarrow 2\ Al^{3+} + SiO_{2(aq)} + 5\ H_2O$	-	1	11.63[d]	−14.09[k]
Goethite	$FeO(OH) + 3\ H^+ \rightarrow Fe^{3+} + 2\ H_2O$	-	6	0.53[b]	−7.90[l]

[a] Aradottir et al., 2012a.
[b] Helgeson 1978, SUPCRT92 (Johnson et al., 1992).
[c] Solubility calculated according to Paul (1977) for the BHVO-2 basaltic glass composition (Wilson, 1997).
[d] Stefansson and Gislasson, 2001.
[e] Povkrosky and Schott (2000).
[f] Schott et al., 1981andSverdrup and Warfvinge, 1988.
[g] Welch and Ullman (2000).
[h] Adjusted fromWhite et al. (1994).
[i] Adjusted from Gislason and Oelkers (2003).
[j] Rimdstidt and Barnes (1980).
[k] Yang and Steefel (2008).
[l] Ruan and Gilkes (1995).

constant for pyroxene in the model is taken from augite measurements (Schott et al., 1981; Sverdrup and Warfvinge, 1988). Kinetics of different plagioclase compositions are available and here we use reference values published for a bytownite composition (Welch and Ullman, 2000). Magnetite dissolution rate parameters are based on the study by White et al. (1994). We used the dissolution rate constant for basaltic glass obtained by Gislason and Oelkers (2003). Precipitation rate parameters for secondary minerals are scarce in the literature, particularly for non-crystalline phases such as allophane and imogolite. For allophane we use the precipitation rate constant measured for amorphous silica precipitation data (Rimstidt and Barnes, 1980). For imogolite we use a precipitation rate constant determined for kaolinite by Yang and Steefel (2008), since imogolite has a Si/Al similar to kaolinite (and lower than allophane). Finally, the dissolution rate data for goethite is derived from Ruan and Gilkes (1995). Acidic and neutral dissolution mechanisms for primary minerals were tested but no differences were found by adding H^+ ion dependence.

After initial experimentation the dissolution rate constants for magnetite and for basaltic glass cited above were both decreased by 1 order of magnitude from the original values to fit the mass loss gradients from the oldest site, Laupahoehoe (20 kyr). We recognize that adjusting dissolution and precipitation rate constants for primary and secondary minerals is far from ideal. However, basing our simulations on laboratory measured values resulted in faster dissolution gradients than the ones observed in all the selected study sites. The discrepancy between slower field observed and faster experimentally determined dissolution rates has long been recognized (White et al., 1996; White and Brantley, 2003; Brantley, 2005; Ganor et al., 2007; Moore et al., 2012).

While mineral surface area (SA) has not been determined for the studied locations, typical values used for modeling weathering of basaltic minerals range between 0.1 to 1 m^2/g, whereas precipitating minerals range up to 10 m^2/g (Dontsova et al., 2009; Navarre-Sitchler et al., 2011; Aradottir et al., 2012a). In our simulations, primary crystalline minerals have smaller reactive surface areas than secondary minerals and glass (Table 2). It is important to note that adjusting mineral surface areas yields identical results to modifying the rate constants for dissolution and precipitation, since rate laws depend linearly on both terms (Eq. (2)).

3.1.3. Aqueous chemistry

Fluxes and composition of the infiltrating rainfall are the same for all simulations, except for the gaseous phases and the organic acids. The model uses dilute rainwater concentrations first reported in White et al. (2009) to model weathering in the Santa Cruz Terrace chronosequence (Table 3). This dataset was chosen because it includes concentrations of elements not commonly analyzed during rainfall chemistry analysis such as Al, Si and Fe. The rainfall hydrochemistry from White et al. (2009) is approximately ten times more concentrated than rainfall at the Thurston site in Hawai'i (Table 3; (NADP/NTN, 2017)).

Table 3
Aqueous chemistry used for initial and boundary conditions in the model (White et al., 2009) and comparison with available rainfall chemistry for the Thurston USGS site.

Species	Concentration (mol L^{-1}) Diluted by 10 × from White et al. (2009)	Concentration (mol L^{-1}) Thurston USGS
$SiO_{2(aq)}$	9.0×10^{-8}	N/A
Al^{3+}	2.0×10^{-8}	N/A
Ca^{2+}	9.0×10^{-6}	8.3×10^{-7}
Mg^{2+}	6.8×10^{-6}	1.9×10^{-6}
Na^{+}	4.2×10^{-5}	1.9×10^{-5}
K^{+}	1.6×10^{-5}	4.9×10^{-7}
Fe^{3+}	1.0×10^{-8}	N/A
Fe^{2+}	1.0×10^{-6}	N/A
Cl^{-}	4.6×10^{-5}	2.3×10^{-5}
SO_4^{2-}	1.6×10^{-5}	1.0×10^{-5}
NO_3^{-}	1.0×10^{-5}	1.1×10^{-6}
pH	5.6	4.7

Thus, all values in White et al. (2009) were diluted by a factor of ten to be incorporated in our simulations. Additionally, we performed a sensitivity test using the available data for the Thurston site and the results are identical to the 10-times diluted rainwater from Santa Cruz. Activity coefficients for all charged aqueous species were calculated using the B-dot model first presented by Helgeson (1969). The B-dot model for activity coefficients is described in Eq. (4):

$$\log\gamma_i = -\frac{Az_i^2\sqrt{I}}{1 + {}_iB\sqrt{I}} + \dot{B}I \quad (4)$$

where I is the ionic strength of the solution, A, B and $\dot{B}$ are and the Debye-Hückel and B-dot parameters taken from the EQ3/6 database (Helgeson and Kirkham, 1974a, 1974b; Helgeson et al., 1981; Wolery, 1992) and $\mathring{a}_i$ is the ion size parameter for each species. No significant differences in the distribution of species were found with respect to assuming activity coefficients equal to 1.

CO_2 is specified to be initially at equilibrium with atmospheric concentrations for infiltrating rainwater at 300 ppmv with no additional CO_2 inputs in the base simulation. A simple approach was taken to reproduce soil carbon respiration by first increasing and fixing the gas flux into the domain to keep up with infiltration and reaction rates (Dontsova et al., 2009; Winnick and Maher, 2018) and second, by elevating the CO_2 fugacity in the column to concentrations that can reach up to 15 × atmospheric values (Fig. A.1, Appendix A). This approach permits modeling an open system that generates an input of CO_2 from the organic matter in the soil profile (Keller and Wood, 1993; Wood et al., 1993; Bacon and Keller, 1998). Molecular oxygen is in equilibrium with the atmosphere for the infiltrating rainwater at 20%. Initially the basalt profile is depleted in O_2, and atmospheric oxygen diffuses to the profile in the same fashion as CO_2.

3.1.4. Organic ligands

LMW organic ligands are important dissolving agents because they can strongly bind to mineral surfaces. Mobility of metal cations is enhanced by LMWOA as they can

form complexes with cations in solutions and soil. Their dissolution-promoting properties are a function of the number of carboxylic groups and dissociation properties of each molecule (Johnson et al., 2004). LMWOA are key to many plant processes such as nutrient uptake under P and Fe-deficient conditions, reduction of Al-phytotoxicity and microbial proliferations (Jones and Darrah, 1994; Jones, 1998; Johnson et al., 2004). Given the high mobility of both Al and Fe and acidic conditions in the LSAG soils, we seek to investigate the weathering impact of LMW organic acids in the system.

We chose to run simulations with oxalic and citric acid because their interactions with aluminosilicate minerals have been well studied and they form stable complexes with Al and Fe (Drever and Stillings, 1997; Stillings et al., 1998; Oelkers and Gislason, 2001; Neaman et al., 2005b; Cama and Ganor, 2006; Olsen and Rimstidt, 2008; Ganor et al., 2009). Previous work by Neaman et al. (2005b) compared the effects of different aliphatic and aromatic organic acids on basalt dissolution. Batch experiments showed that citrate, a tridentate ligand, is the most effective ligand to release all cations including Si, and it particularly enhances the release of Fe. Oxalate – a bidentate ligand – proved to be the second most effective leaching agent. Aromatic ligands such as succinate or salicylate were less effective compared to citrate and oxalate. Analogous results were obtained by Li et al. (2006) showing that Al mobility is enhanced by citric and oxalic acids when compared to other similar compounds. The differences in behavior of citrate and oxalate on Fe leaching can be explained due to differences in the stability constants for Fe-citrate and Fe-oxalate complexes. In contrast, Al-citrate and Al-oxalate complexes show comparable leaching rates because of their similar thermodynamic stability. Thus, Al leaching in the presence of citric and/or oxalic acids is controlled by the total concentration of each or both LMW organic acids (Li et al., 2006). This response agrees with reactive transport simulations of granite weathering by Lawrence et al. (2014). Their study tested the coupled effect of three LMW organic acids (oxalate, citrate and acetate) in Al losses from granitic weathering profile. They found that oxalate-exclusive and combined-ligands simulations showed similar behavior for Al.

For the simulations that include LMW organic acids, citrate and oxalate are added in the infiltrating fluid with initial rainfall composition. This approach aims to reproduce the production of organic exudates in the rhizosphere which are rapidly transported due to high conductivity and fast flow in the model system. A broad range of concentrations of LMWOA in soils has been reported ranging from 0.1 μM to 300 μM for most common acids, such as oxalic, citric, malic, acetic and lactic acids (Fox and Comerford, 1990; Strom et al., 1994; Jones, 1998; van Hees et al., 2000; van Hees et al., 2003; van Hees et al., 2005). Oxalate and citrate concentrations in soil solutions from tropical montane forest soils have been reported to be between 0.1 up to 60 μM in younger P-rich soils and older P-deficient soils respectively (Aoki et al., 2012; Fujii et al., 2012). We ran simulations within 0.01 to 100 μM to estimate the concentration of organic ligands to use for our model. Citrate and oxalate concentrations for the organic ligands' simulation M3 were set at 100 μM. This is a two-fold increase compared to the highest values obtained by Fujii et al. (2012), which is justified by the lower soil pH values and higher soil C in the 20-kyr soils from Laupahoehoe. In our simulations, only Fe(III) and Al can form complexes with oxalate and citrate and their respective stability constants are shown in Table 4. These values were obtained from the Minteq thermodynamic database (Morrey et al., 1985) and are based on the original work by Sposito and Mattigold (1980) for their GEOCHEM code. Complexation with other metals in the system was not included.

We discussed previously the importance of using internally consistent thermodynamic data because combining thermodynamic databases can lead to misleading results when these have not been developed from the same original sources. This caveat is also true for data of aqueous species (Oelkers et al., 2009; Wolery and Colon, 2017). The Al-oxalate complexes equilibrium constants in the Minteq database are different from the values included in the LLNL database which are derived from Prapaipong et al. (1999). However, it was important for this study to include Al, Fe(III) citrate and Fe(III)-oxalate complexes that are not available in the LLNL database neither in the SUPCRT92 package. Thus, before combining the Minteq database with the extended LLNL database used here, we ran a simulation with only Al-oxalate complexes for both databases. We confirmed that there are not significant differences for Al-species activities and Al concentrations in the solid among the two datasets. This assessment gives us confidence about the Al-oxalate thermodynamic data consistency, but we have to make the assumption that this result can be extrapolated to the missing thermodynamic data – Al and Fe(III) citrate and ferric-oxalate. Consequently, all the ligand stability constants used in this study for the LMWOA simulation are derived from the Minteq database instead of mixing the Al-oxalate data from LLNL with Minteq values.

3.1.5. Aqueous Kinetics

Basaltic rocks in Hawaiian volcanoes can host up to 8% wt. of iron, with $FeIII/\sum Fe \approx 0.15$ (Moussallam et al., 2014; Brounce et al., 2017; Helz et al., 2017); ferric iron is usually present in spinels like magnetite and ilmenite. Dissolution equations of primary minerals in our simulations are described in terms of Fe^{2+}, with no other mechanism describing the oxidation of Fe besides equilibrium between the iron redox pair. Therefore, we incorporate an aqueous reaction to oxidize ferrous to ferric iron in the presence of molecular O_2. In this set of simulations, we have tested two types of aqueous kinetic rate laws to describe iron oxidation by O_2 in the system. According to Singer and Stumm (1970) the Fe^{2+} oxidation is described by two rate-laws: a neutral-mechanism with no dependence on pH and an acid-mechanism dependent on pH. For the first set of simulations (M1, M2, M3) we incorporated only the TST-linear rate law with no dependence on inhibiting or promoting species:

$$R = k_{neutral} a_{Fe^{2+}} a_{O_2} \left(1 - \frac{Q}{K}\right) \quad (5)$$

Table 4
Standard state dissociation constants for oxalate and citrate complexes with Fe(III) and Al used in the organic ligands simulation (M3).

Complex reaction	Log $K_{eq,25\ °C}$
$Fe\text{-}Oxalate^{+} \rightarrow Fe^{3+} + Oxalate^{2-}$	−9.15
$Fe\text{-}(Oxalate)_2^{-} \rightarrow Fe^{3+} + 2\ Oxalate^{2-}$	−15.45
$Fe\text{-}(Oxalate)_3^{-} \rightarrow Fe^{3+} + 3\ Oxalate^{2-}$	−19.83
$Fe\text{-}Citrate_{(aq)} \rightarrow Fe^{3+} + Citrate^{3-}$	−13.13
$Fe\text{-}H\text{-}Citrate^{+} \rightarrow Fe^{3+} + H^{+} + Citrate^{3-}$	−10.17
$Fe\text{-}(OH)\text{-}Citrate^{-} + H^{+} \rightarrow Fe^{3+} + Citrate^{3-} + H_2O$	−1.79
$Al\text{-}Oxalate^{+} \rightarrow Al^{3+} + Oxalate^{2-}$	−7.73
$Al\text{-}(Oxalate)_2^{2-} \rightarrow Al^{3+} + 2\ Oxalate^{2-}$	−13.41
$Al\text{-}(Oxalate)_3^{3-} \rightarrow Al^{3+} + 3\ Oxalate^{2-}$	−17.09
$Al\text{-}H\text{-}Oxalate^{2+} \rightarrow Al^{3+} + H^{+} + Oxalate^{2-}$	−7.46
$Al\text{-}(OH)\text{-}Oxalate_{(aq)} + H^{+} \rightarrow Al^{3+} + Oxalate^{2-} + H_2O$	−2.57
$Al\text{-}(OH)\text{-}(Oxalate)_2^{-} + H^{+} \rightarrow Al^{3+} + 2\ Oxalate^{2-} + H_2O$	−6.84
$Al\text{-}(OH)_2\text{-}Oxalate^{-} + 2H^{+} \rightarrow Al^{3+} + Oxalate^{2-} + 2H_2O$	3.12
$Al\text{-}Citrate_{(aq)} \rightarrow Al^{3+} + Citrate^{3-}$	−9.98
$Al\text{-}(Citrate)_2^{-} \rightarrow Al^{3+} + 2\ Citrate^{3-}$	−14.83
$Al\text{-}H\text{-}Citrate^{+} \rightarrow Al^{3+} + H^{+} + Citrate^{3-}$	−12.85

Thermodynamic data from Minteq database (Morrey et al., 1985)

However, because pH is higher at the younger stages, it is expected that the acid mechanism described by Singer and Stumm (1970) dominates Fe oxidation rates because its dependence on the square of pH (Eq. (6)). Thus, we also evaluate the case in which Fe oxidation is controlled by a parallel rate-law that considers the sum of both neutral and acid mechanisms as described by Singer and Stumm (1970). The total parallel rate is the sum of the neutral and acid rate laws (Eq. (7)).

$$R = k_{acid}\frac{a_{Fe^{2+}}a_{O_2}}{a_{H^+}^2}\left(1-\frac{Q}{K}\right) \tag{6}$$

$$R = k_{neutral}a_{Fe^{2+}}a_{O_2}\left(1-\frac{Q}{K}\right) + k_{acid}\frac{a_{Fe^{2+}}a_{O_2}}{a_{H^+}^2}\left(1-\frac{Q}{K}\right) \tag{7}$$

Given the incorporation of LMWOA to our weathering models, it is important to capture the fate and distribution of these molecules. LMWOA are decomposed by oxidation and are usually short-lived in soil (Jones and Darrah, 1994; Jones, 1998; van Hees et al., 2005). Dissolved LMW organic ligands have the highest concentrations at the surface horizons of the soil profile. The concentration of dissolved organic acids decreases with depth because of decomposition during transport to lower horizons, adsorption to mineral surfaces and occlusion and aggregation with secondary phases. To represent the decomposition of LMWOA in our simulations we follow the approach taken by Lawrence et al. (2014). A first-order rate depending on the concentration of the organic ligand is used for both oxalate and citrate. Therefore, the change in oxalate or citrate concentration depends on the concentrations of the total acid and a decomposition rate constant set to −0.5 mol L^{-1} yr^{-1}. Oxidation of two moles of oxalic acid consumes one mole of O_2 and produces four molecules of CO_2 (Eq.(8)), while the oxidation of two moles of citric acid consumes nine moles of O_2 and produces 12 moles of CO_2 (Eq. (9)). This is implemented as an irreversible rate for oxalate and citrate decay in CrunchFlow.

$$2H_2C_2O_4 + O_2 = 4CO_2 + 2H_2O \tag{8}$$

$$2H_8C_6O_7 + 9O_2 = 12CO_2 + 8H_2O \tag{9}$$

3.2. Model formulation

The essentials of our simulations consist of a one-dimensional 1 meter "fresh" basalt column comprised of 50 nodes of 2 cm each. The porous basalt column reacts with infiltrating rainfall water and gases, each transported by advection and diffusion respectively with a maximum time-step of 1 year. Model simulations are run with an implicit solver for 20,000 years and spatial profiles are obtained at 0.3 and 20 kyrs to compare with data available for 1 meter of soil/bedrock material – the Thurston (0.3 kyr) and Laupahoehoe (20 kyr) sites previously described (Fig. 1). Aqueous and gaseous species at the land–atmosphere interface are modeled by a Dirichlet boundary condition, whereas the base of the rock/soil profile is modeled by a flux boundary condition. Temperature of the models was set at 25 °C despite annual MAT in the areas is 16 °C. We did run a test simulation at 16 °C to confirm that the effect of temperature in the system is insignificant.

3.2.1. Transport

Aqueous flow is modeled exclusively as vertical infiltration by 1-D Darcy flow. Initial porosity is set up to 30%, a conservative estimate for matrix and fracture porosity of young basalts (Saar and Manga, 1999). No attempt was made to account for any differential advection (preferential flow) that may exist in these sites. Cooling joints and fractures, lava tubes and channels are common in volcanic lava flows and pyroclastic deposits of basaltic composition (Lau and Mink, 2006). The heterogeneous nature of these features is difficult to characterize in a 1-D reactive transport model. However, 1-D Darcy flow is a good approximation because of the ashy nature of soils in the younger site which minimizes this effect and reduced hydraulic conductivity

from preferential flow features in the older site (Lohse and Dietrich, 2005). Yet some degree of preferential flow persists in these older Hawaiian soils (Marin-Spiotta et al., 2011).

Rainfall infiltration fluxes are estimated using a mass balance between rainfall and evapotranspiration and assume partial lateral runoff. Mean annual precipitation is equal to 2.5 m/yr and potential evapotranspiration is close to 50% for this system (Engott, 2011; Giambelluca et al., 2013). After accounting for ET and runoff losses the calculated infiltration flux is 1.06 meters per year. Even though MAP in these sites is high, unsaturated conditions in Hawaiian weathering soils are typical due to the high hydraulic conductivity of the system (Lohse and Dietrich, 2005) and episodic rainfall events, hence, most simulations were run at unsaturated conditions. Soil moisture measurements range between 30 and 70% wt. (Fig. A.1), accordingly we run simulation at 30, 50 and 70 percent saturation plus at fully saturated conditions.

4. RESULTS

Our simulations are constructed from a base model (M1) that only includes rainfall infiltration under partially saturated flow conditions. Each of the scenarios studied (variable saturation at atmospheric P_{CO2}, high soil P_{CO2}, organic ligands) are incorporated sequentially, yielding a total of three classes of simulations. We present and discuss soil pore water pH and mass-transfer profiles for Al, Fe, Si, Ca and Mg; these variables allow us to characterize weathering extent in the system. We assume that soil pore water pH is equivalent to soil pH measured in the LSAG sites in lack of pore water information. Thus, from here on we use these terms interchangeably. Al, Si and Fe characterize mineral transformations occurring in the system: dissolution of primary minerals, and precipitation of amorphous secondary silicates and Fe(III)-oxyhydroxides. Ca and Mg are indicative of changes in soil buffering capacity and nutrient availability. These variables respond differently to the weathering agents studied. Sensitivity analyses regarding degree of saturation, concentration of CO_2 and organic ligands, and different dissolution rate-law formulations are included in the Appendix B.

4.1. Calculation of mass-transfer profiles and parent material selection

To compare our reactive transport modeling results to the LSAG data, mass-transfer coefficients are calculated from elemental concentrations from both chronosequence and models. Mass transfer coefficients show the fractional enrichment or depletion of an element relative to a parent material normalized to an immobile element (Equation (10)).

$$\tau_{j,w} = \frac{C_{j,w} C_{Nb,p}}{C_{Nb,w} C_{j,p}} - 1 \tag{10}$$

The mass-transfer coefficient $\tau_{j,w}$ for element j, is calculated by the concentration of j in the weathered material $C_{j,w}$ and parent material $C_{j,p}$, relative to niobium, the immobile component Nb in the weathered and parent material, $C_{Nb,w}$ and $C_{Nb,p}$ respectively (Brimhall and Dietrich, 1987; Chadwick et al., 1990). Niobium was chosen to calculate the mass-transfer coefficients since Kurtz et al. (2000) demonstrated Nb is the least mobile element in these soil sites. Positive $\tau_{j,w}$ values indicate enrichment of an element, whereas negative $\tau_{j,w}$ denote element depletion.

Parent material for the Thurston (0.3 kyr) site is based on samples from the C-horizon at the bottom of the soil pit, where unaltered bedrock was observed (Kurtz et al., 2000; Vitousek et al., 1997). Conversely, the Laupahoehoe 20 kyr site is developed in a thin blanket of tephra and coring down to 1 meter of unweathered rock does not necessarily represent the soil parent material, and (Kurtz et al., 2000) concluded that the parent material for the Laupahoehoe site is somewhat uncertain. Given this issue, for the Laupahoehoe parent material we use the data from Bateman et al. (2018 – Ecosystems in revision). This later study in a drier portion of the rainfall gradient in the Laupahoehoe site was able to recover a more suitable parent material for the soils developed from the final alkalic stage of Mauna Kea eruptions. We also compared these data normalizing to BHVO-2. Significant differences in the mass-transfer coefficients are observed for Mg and Fe, which is expected for variation in these elements between the alkalic and tholeiitic series, and because Nb concentrations vary between Hawaiian tholeiitic and alkali basalts.

Mass-transfer coefficients are widely used in the study of soils, but uncertainties and the effects of heterogeneity in parent materials can be hard to quantify. Here, we have estimated the uncertainty in the composition of the parent material for these sites to range between 10 to 30% (Fig. C.1).

4.2. Base simulation (M1)

The base reactive transport model consists of a 1-m weathering basalt profile, infiltrated by rainfall fluid, in which transport occurs under 50% saturation. The infiltrating fluid is initially at equilibrium with atmospheric $CO_2 = 3 \times 10^{-4}$ and $O_2 = 0.2$ atm, while the initial concentrations of CO_2 in the porous media is the same and O_2 is set to 10^{-8} atm. Besides equilibrium with atmospheric gases in the infiltrating fluid, there are no additional sources of CO_2. LMW organic acids and complexation with Al and Fe are absent from the simulation.

Soil water pH rapidly increases due to the high buffering capacity from basalt weathering (Fig. 2a). In the first 0.3 kyr, pH is rapidly buffered above pH = 10 along the whole weathering profile. Continued water flux for the next 20 kyr allows pH to drop down to 6 at the top of the profile. However, it continues to be buffered to pH > 9 below the topmost 15 cm at 20 kyr. The base model fails to capture the pH values observed in the LSAG sites: it predicts values 5 pH units higher than measured; and shows a shallow weathering front in the first 10 centimeters that is not observed at the Laupahoehoe site. Essentially the system is acid-limited.

High pH values predicted by the base model dominate the behavior of the elemental profiles. Aluminum shows

losses in the first 20 cm at all weathering stages (Fig. 2b). At 0.3-kyr Al is immobile below the uppermost 20 cm. Leaching of Al continues over the next 10-kyr, reaching nearly constant losses below 40 cm by the 20-kyr stage. The highly alkaline pH's (>9) along the profile, promote dissolution plagioclase and the basaltic glass (Fig. B.1), which results in elevated total Al concentrations in the fluid but low free Al^{3+} activity (Fig. B.2). AlO_2^- is the most abundant species at these high pH's, followed by $Al(OH)_4^-$ (Fig. B.2). After 20 kyr these simulations produce small (15%) losses below 40 cm, while the Laupahoehoe soil data show much more extensive Al loss (~50%). Iron stays constant in the simulated profile at 0.3 kyr. At 20 kyr, Fe decreases with a gradual weathering front. Below this weathering front, Fe remains constant with ~ 10% losses (Fig. 2c). Incomplete dissolution of Fe-bearing primary phases at elevated pH's causes restricted Fe losses for the M1 simulation; magnetite is insoluble (the ion activity product $IAP \geq 0$) in the profile while olivine and pyroxene are undersaturated only in the top 20–30 cm (Fig. B.1). The field data shows larger integrated larger Fe losses (>50% at 20 kyr) that are not captured in this simulation.

Fig. 2(d-f) shows the base model results for Si, Ca and Mg. The model predicts Si losses for all stages of weathering. The Si profile for M1 develops a gradual weathering front observed at all weathering stages. Si losses in the top 10–30 cm range between 35–85% at 0.3 and 20 kyr respectively. Below the weathering front, Si is immobile at 0.3 kyr and progresses to 50% loss by 20-kyr. The model M1 underestimates total Si losses at 20 kyr, while the weathering front does not move downwards with age. Magnesium is lost in the model; it shows a distinctive gradual

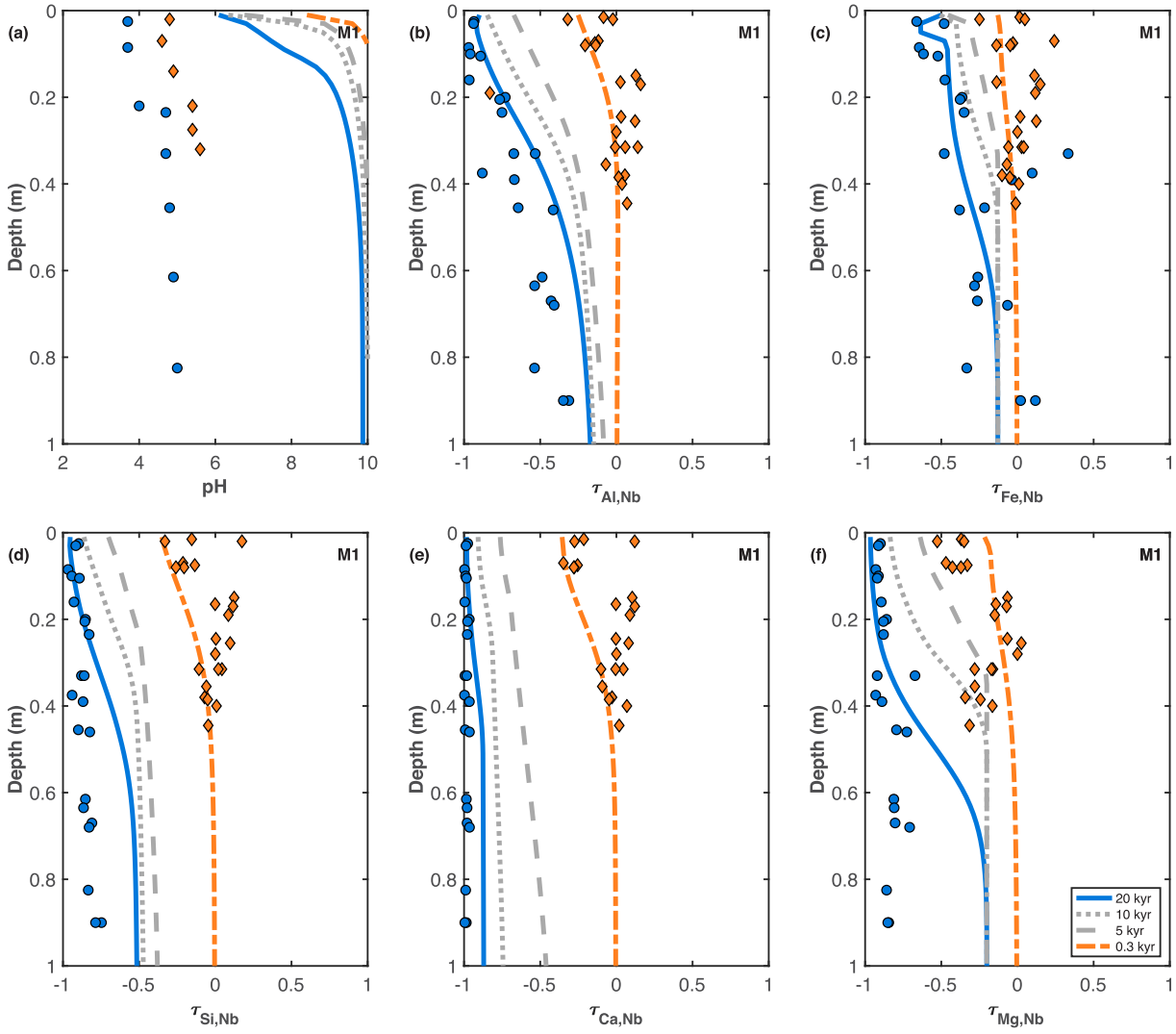

Fig. 2. M1 (base) model weathering profiles: infiltrating fluid is rainfall at equilibrium with atmospheric CO_2 (300 ppmv). Profiles show modeled profiles for (a) pH, (b) Al mass-transfer coefficient $\tau_{Al,Nb}$, (c) Fe mass-transfer coefficient $\tau_{Fe,Nb}$, (d) Si mass-transfer coefficient $\tau_{Si,Nb}$, (e) Ca mass-transfer coefficient and (f) Mg mass-transfer coefficient $\tau_{Mg,Nb}$, as a function of depth at 0.3 (orange-dot-dashed line), 5 (gray-dashed line), 10 (gray-dotted line) and 20 (blue-solid line) kyr. LSAG data is shown as orange diamonds for Thurston (0.3 kyr) and as blue circles for Laupahoehoe (20-kyr) (Vitousek et al., 1997; Hedin et al., 2003; Vitousek, 2004).

weathering front that propagates downwards by 25 cm by every 10 kyr, sitting at 50 cm depth by the 20 kyr stage. The model results agree reasonably well with observations in the upper 20–40 cm for all sites but diverge at greater depth. Below 50 cm, M1 underestimates Mg losses at 20 kyr. This result emulates the Fe profile because of partial dissolution of the Mg-bearing phases (pyroxene, olivine) at high pH's (Fig. B.1). Calcium in the model begins to be exported at 0.3-kyr and shows a shallow gradient at 10 cm. At 20 kyr, Ca is not completely exported from the profile, with at least ~10% remaining below 60 cm. Finally, although the model performs better for Ca than for Si or Mg; it does not capture the near-complete depletion at the oldest stage as observed in Laupahoehoe (20 kyr).

4.2.1. Sensitivity analyses: water-column saturation

Different degrees of water-column saturation can alter reactions sensitive to pH and oxygen fugacity. We tested two more scenarios with varying degrees of water-column saturation in the profile at 30% saturation and a closed-system in which the domain is fully saturated. Varying soil water saturation conditions changes the pH profile at 20-kyr by developing slightly deeper and more gradual weathering fronts as water saturation decreases. pH is buffered below the weathering front to identical values for the closed and open systems at varying degrees of water saturation (Fig. B.3). Since changes in pH are so limited, minimal variations were observed for the element distribution profiles, so no additional figures are included for these. The saturated system (equivalent to a closed system) can significantly limit CO_2 diffusion in the profile: throughout the column P_{CO2} increases as the as water saturation decreases. However, since P_{CO2} is low and there are no additional sources of CO_2 in the base simulation, carbon dioxide is rapidly consumed by mineral dissolution despite decreasing soil water content.

4.3. Increased and constant CO_2 as soil respiration (M2)

Soil respiration contributes to a flux of CO_2 that can lead to soil P_{CO2} up to 2 orders of magnitude greater than atmospheric (Fig. A.1), (Wood et al., 1993). Soil carbon stocks are 10 and 60 kg/m^2 at the youngest Thurston and oldest Laupahoehoe sites respectively (for the upper 20 cm). O-horizon carbon content increases from 10% in the youngest soils up to 40% carbon in Laupahoehoe (Crews et al., 1995; Torn et al., 1997). Large stocks of organic carbon imply that respiration of soil organic matter produces high CO_2 fluxes. As a point of reference, we use soil CO_2 concentration and surface efflux in older Hawaiian soils (150 and 400 kyr), with comparable vegetation to the Kona and Laupahoehoe sites. Soil CO_2 concentrations range from 480 ppmv near the surface to 6300 ppmv at 60 cm depth, while flux rates range between 1.6–14.2 μmol m^{-2} s^{-1}. Soil CO_2 follows a reaction-diffusion model with diffusivity of 0.04 cm^2 s^{-1}, reaching up to 15 times atmospheric CO_2 levels (Fig. A.2).

To assess the importance of soil respiration in weathering of Hawaiian soils, a constant elevated flux of CO_2 (and O_2) is prescribed in this simulation. In the M2 model we increase CO_2 as a product of soil respiration by equilibrating the infiltrating fluid (rainfall) with higher atmospheric carbon dioxide concentrations: CO_2 fugacity was increased tenfold from atmospheric CO_2 up to 3000 ppmv. This is a conservative estimate since observations from similar Hawaiian soils indicate CO_2 concentrations can exceed 5000 ppmv at depth (Fig. A.1).

The effect of high P_{CO2} on soil pH in the simulation is important (Fig. 3a). At the 0.3-kyr stage pH is no longer buffered above 10 as the previous simulations, and only becomes more basic at the bottom of the profile ($8 < pH < 9$). With time, pH continues to decrease along the weathering column. By 10 kyr it reaches pH values below 7 for the whole profile. At 20-kyr pH is slightly acidic along the whole profile, gradually increasing from 5.2 at the top to 6.8 at the bottom. Incorporating soil respiration does achieve a major reduction in soil pH, but the M2 model cannot achieve the lower soil pH observed in the older, intensively weathered soils (e.g. Fig. A.1). Circumneutral pH's result in immobility of Al along the profile (Fig. 3b). At all weathering stages mass-transfer coefficients for Al stay near zero, showing no accumulation nor depletion for the 1-m weathering column. Immobility of Al in this weathering scenario is the result of continuous precipitation of allophane and imogolite, as they stay supersaturated throughout the weathering profile (Fig. B.4). The constant flux of CO_2 plus the ten-fold increase in soil P_{CO2} in the M2 simulations reduces Al mobility relative to M1, where CO_2 limitation led to alkaline conditions that promoted Al loss but otherwise failed to reproduce important features of the weathering profiles (Figs. 2 and 3).

The constant flux of oxygen and carbon dioxide cause major changes in Fe distribution along the basalt column at 10 and 20 kyr (Fig. 3c). A sharp and small weathering front is developed, moving from 25 to 50 cm at 5 and 10 kyr respectively. After 20 kyr of weathering, Fe losses are constant along the profile (~60%). The distribution of total Fe in this model can be explained by dissolution of pyroxene, olivine and particularly magnetite ($IAP < 0$), allowing goethite to precipitate as it becomes slightly supersaturated (Fig. B.4). However, goethite precipitation cannot keep up with dissolution of the primary Fe-bearing phases. There are significant changes for Si, Ca and Mg with respect to the M1 simulation (Fig. 3d-f). All weathering profiles become vertical at 5, 10 and 20 kyr, with no gradient on their weathering fronts. Mg and Ca are totally depleted by 20 kyr as measured in the Laupahoehoe site; whereas Si is not completely lost, with 20% remaining by 20 kyr. The vertical tau profiles for Mg and Ca losses at 20-kyr illustrate dissolution of all primary phases in M2 (Fig. B.4).

4.4. Incorporation of organic ligands (M3)

As discussed previously, organic ligands can be important weathering agents in organic-rich soils like the ones developed in the Island of Hawai'i. We argued that these soils have high concentrations of organic matter and thus respiration is a key factor in speeding up reaction rates via increasing P_{CO2}. But biologic activity will also increase the concentrations of LMW organic ligands in the system,

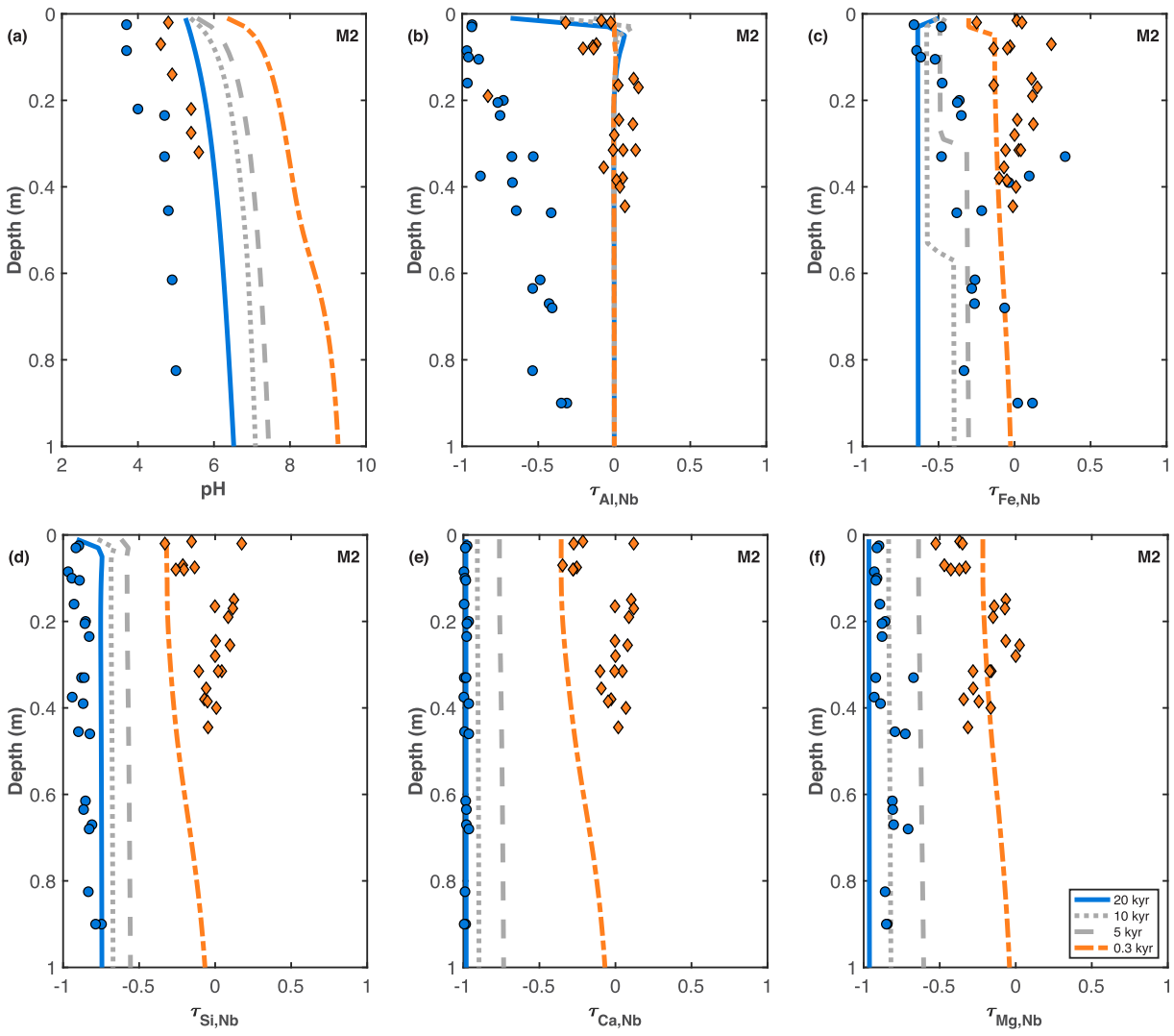

Fig. 3. M2 model weathering profiles: soil respiration modeled by increased and constant CO_2 flux. Profiles show (a) pH, (b) $\tau_{Al,Nb}$, (c) $\tau_{Fe,Nb}$, (d) $\tau_{Si,Nb}$, (e) $\tau_{Ca,Nb}$ and (f) $\tau_{Mg,Nb}$ as a function of depth at 0.3, 5, 10 and 20 kyr. Legend and symbols are the same as Fig. 2.

where they can be critical weathering agents in the Hawaiian regolith.

By adding organic acids to the model, the pH is effectively lowered in all weathering stages when compared to the rest of simulations. The addition of 100 μM of oxalate and citrate to the infiltrating rainfall results in the best-fitting modeled chemistry at the 20-kyr phase for all elements and pH. During the first 0.3 kyr, pH at the surface is 3.9 followed by rapid buffering above pH 7 (Fig. 4a). The M3 simulation shows that the pH weathering front moves deeper with age. After 20 kyr, pH at the surface stays at 3.7 and the weathering front propagates downwards becoming less steep. When compared to the available pH data, this simulation reproduces the low soil pH measured at the Laupahoehoe (20 kyr) site from top to bottom. The discrepancy in pH between the organic ligand model and the Thurston site is the result of simplifications in our model which assume no interaction with acidic volcanic gasses at the earliest stage and addition of organic acids since the initiation of the model, which would be prior to onset of significant microbiological and plant activity. We tested the M3 simulation with a sequential onset of organic acids at a later stage (at 2kyr) but found that it only resulted in a minor pH shift at the 10 kyr stage and no significant alteration on the elemental distribution profiles.

The modeled distribution of Al in the profile captures key distinctive features measured in the chronosequence sites: immobility at the Thurston 0.3-kyr site; and sustained losses in the 20 kyr site (Fig. 4b). By 0.3 kyr, mass-transfer values show losses (<20%) in the topmost 5 cm while staying constant below this depth. Al continues to be removed from the profile in the next 10 kyr: the first 5 cm show losses between 75–90%, decreasing with depth below this level; whereas at 40 cm Al begins to increase in the profile, with 20% gains principally from imogolite precipitation (Figures B. 5 and B. 6). At the 20 kyr stage Al continues to be leached from the basalt; only 10% of the initial Al remains in the uppermost 25 cm. From this

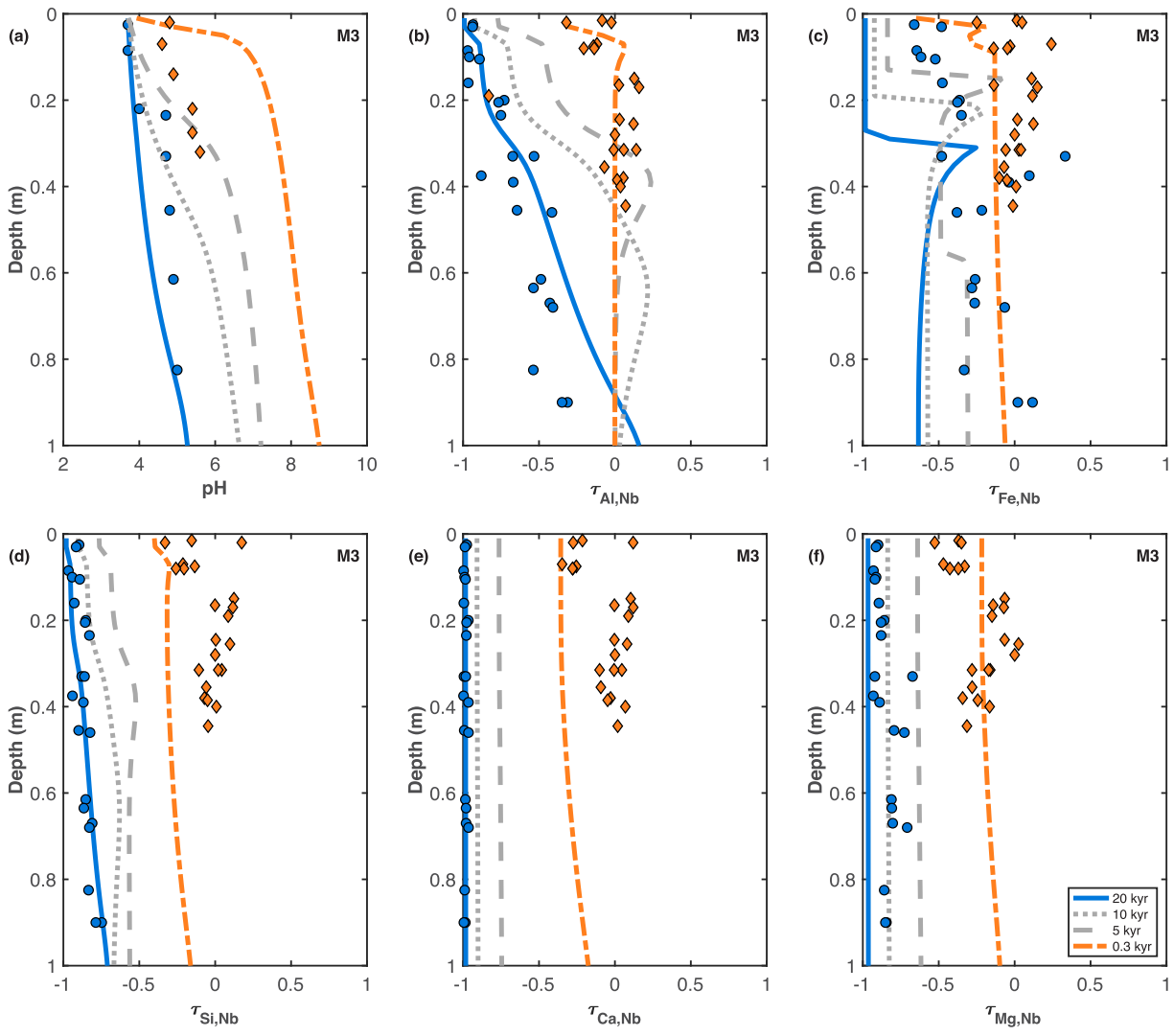

Fig. 4. M3 model weathering profiles: 100 μM of citrate and oxalate added to infiltrating fluid, plus soil respiration (increased CO_2 flux). Profiles show (a) pH, (b) $\tau_{Al,Nb}$, (c) $\tau_{Fe,Nb}$, (d) $\tau_{Si,Nb}$, (e) $\tau_{Ca,Nb}$ and (f) $\tau_{Mg,Nb}$ as a function of depth at 0.3, 5, 10 and 20 kyr. Legend and symbols are the same as Fig. 2.

point, Al gradually increases with depth until there are negligible losses below 95 cm. The Al losses are achieved by complete dissolution of primary minerals followed by partial dissolution of secondary allophane and imogolite (Figures B. 5 and B. 6). The M3 model overestimates Al content below 20 and 60 cm at the 20 kyr site. The fluid becomes closer to saturation with respect to allophane and imogolite, which reduces the reaction rates (Fig. B.5) below this depth due to pH values above 4.2 and increased activity of free Al^{3+} (Fig. 5). Faster fluid transit times could result in a better estimation of Al abundance in the profile. Alternatively, oxalate and citrate decomposition could also cause the small overestimation of Al in the profile after 20 kyr of weathering. We ruled out this possibility by running M3 without decomposition rates for both LMWOA, which resulted in no significant differences for pH and Al (and all other elements) distribution in the weathering profiles.

For the modeled Fe distribution, the M3 simulation is not able to correctly calculate its abundance in the profile at 20 kyr but does capture the shape of the Fe distribution (Fig. 4c). Modeled Fe stays mostly immobile in the profile at the 0.3 kyr stage with mass losses restricted to the surface. During the following weathering stages, Fe develops a distinctive weathering profile: total depletion at the top followed by a steep reaction front and accumulation peak that gradually decreases towards the bottom. By 20 kyr, Fe is totally lost in the topmost 30 cm and both the weathering front and accumulation peak propagate downwards from the previous stage. Below the accumulation peak, Fe losses are uniform and equivalent to the 10 kyr stage, staying at 60% Fe losses down to 1 meter depth. As primary Fe-bearing phases are completely dissolved at these later stages, the Fe profile mirrors the behavior of goethite; becoming unsaturated in the profile at pH < 3.9 (Fig. 4, B. 5 and B. 6). Compared to the data, the M3 simulation can reproduce

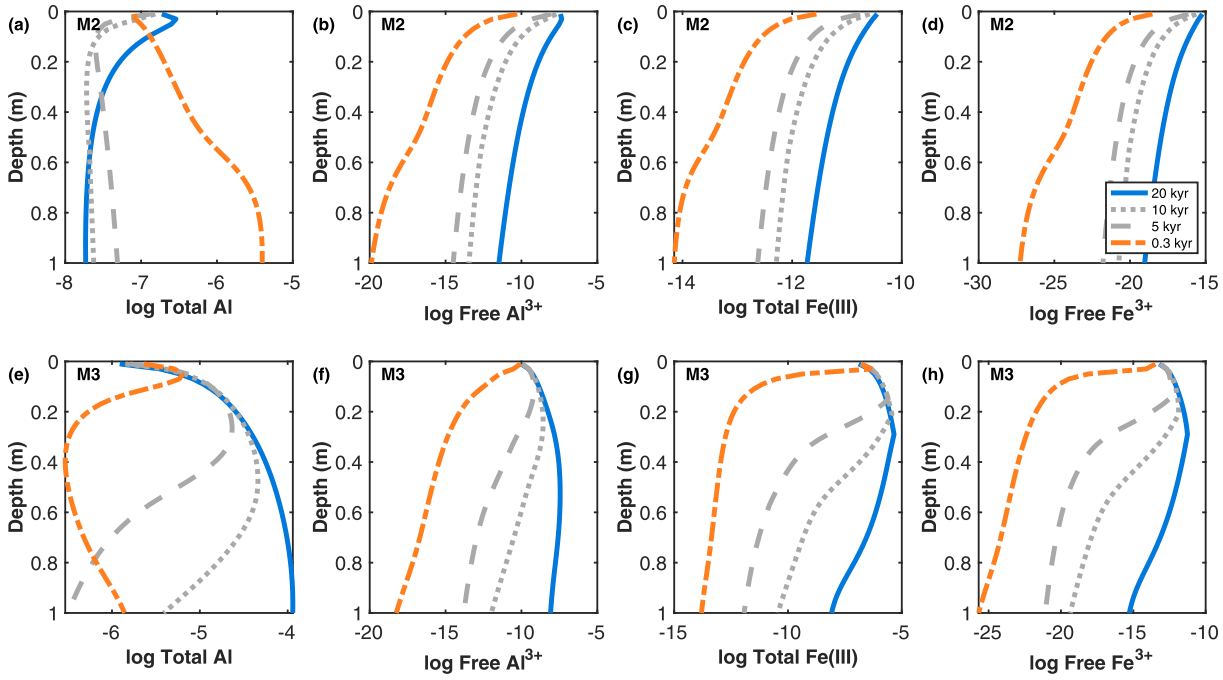

Fig. 5. Temporal evolution of Al and Fe(III) fluid concentrations in models M2 (a-d) and M3 (e-h). Panels (a) and (e) show sum of total Al species; (b) and (f) dissolved Al^{3+} activities; (c) and (g) sum of total Fe(III) species; (d) and (h) dissolved ferric iron (Fe^{3+}) activity as a function of depth, at 0.3 (orange dot-dashed line), 5 (gray dashed line), 10 (gray dotted line) and 20 kyr (blue solid line).

the accumulation peak recognized at the Laupahoehoe site and captures the magnitude and distribution of losses for the Laupahoehoe site. But the model exaggerates Fe losses in the top 30 cm of the weathering profile when compared to the 20 kyr data. These discrepancies can be attributed to the early and continuous input of organic acids, which appears to decrease pH and the activity of dissolved Fe^{3+} more quickly than indicated by the soil observations (Fig. 5).

In the M2 simulation (Fig. B.5) Ca and Mg are totally depleted by 20 kyr, and no changes are observed when organic ligands are incorporated to the model. However, the addition of organic acids in M3 does result in relevant shifts for Si (Fig. 4): the Si weathering profile develops a gradual weathering front. For Si, the organic ligand simulation achieves losses greater than 90% at 20 kyr for most part of the profile. However, it overestimates the abundance of Si towards the bottom, similar to the behavior of Al in the profile which responds to only partial dissolution of allophane and imogolite (Figures B. 5 and B. 6) and does not quite reach the vertical distribution of Si at Laupahoehoe, with >90% uniform losses.

4.4.1. Distribution of Al and Fe(III) organic complexes

After analyzing the overall effect of LMWOA in fast chemical weathering, we now examine the individual temporal and spatial distribution of Al and Fe(III) citrate and oxalate complexes. Model M3 shows that complexation of oxalate and citrate with Al and Fe(III) behaves differently with time along the weathering profile (Fig. 6). For Al, at the higher pH's in the 0.3 kyr weathering stage Al readily associates with oxalate while Al-citrate complexes are abundant only near the surface. The abundance of Al-oxalate complexes increases with time and by 20 kyr mean log (ΣAl-oxalate) = $10^{-4.5}$ M, meaning that almost all oxalate is forming complexes with Al. Al-citrate complexes show a different pattern by rapidly increasing with time and becoming more abundant than oxalate by 20 kyr (mean log (ΣAl-citrate) = $10^{-4.3}$ M). Both Al-citrate and Al-oxalate complexes decrease in the top of the profile at 20-kyr as pH goes below their respective second pKa's (4.76 for citrate and 4.14 for oxalate) (Figure B.7). Fe(III) complexation shows different patterns with both organic ligands, as Fe(III)-citrate complexes are slightly more abundant than Fe(III)-oxalate for all stages of weathering (Fig. 6). However, when compared to Al, Fe(III) complexes are less abundant since concentration of total dissolved Fe(III) in the fluid is smaller than total dissolved Al (Fig. 5). At the top of the profile at the 10 and 20-kyr weathering stages, Fe(III) complexes with citrate and oxalate also decrease when pH goes below their pKa's (Figure B.7). Based on these results, oxalate is the most efficient ligand for aluminum mobilization at a wider range of pH's (especially at neutral and slightly basic pH's), but citrate is the most important ligand for Al at the pH range between its second and third dissociation constants ($pKa_2 = 4.76$ and $pKa_3 = 6.39$). Fe(III) mobilization is greater at all times with citrate, however oxalate shows a similar capacity to mobilize ferric iron and at lower pH's it is comparable to citrate.

4.5. Alternative rate-laws for mineral dissolution and iron oxidation

4.5.1. Al-inhibition rate-law

We tested the Al-inhibition rate-law on the organic ligand simulation M3 (Eq. (3)). According to this formulation

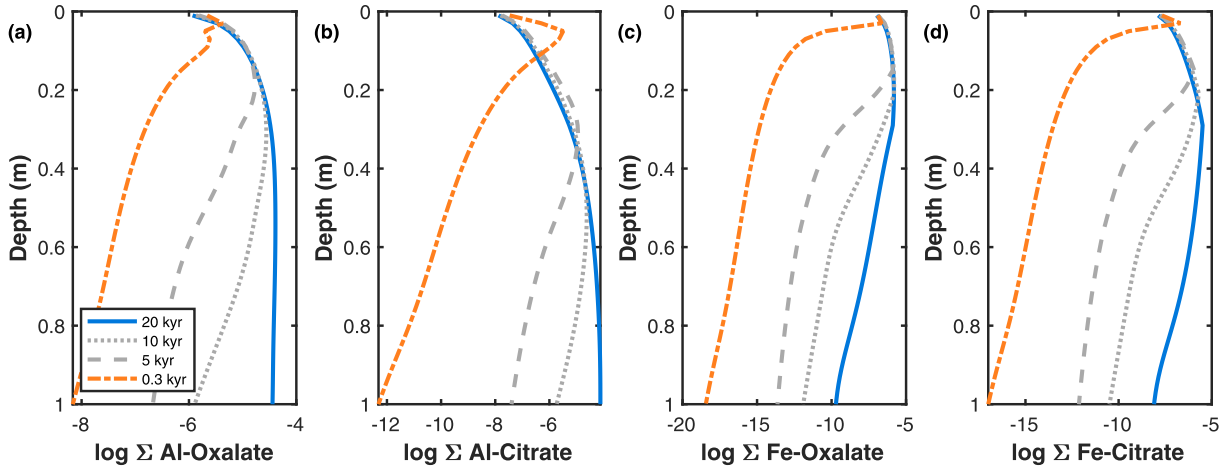

Fig. 6. M3 modeled sum of aluminum and ferric iron organic species. Panel (a) shows the sum of Al-oxalate species. (b) Sum of Al-citrate species. (c) Sum of Fe(III)-oxalate species. (d) Sum of Fe(III)-citrate species. Modeled profiles are shown at 0.3 (orange dot-dashed line), 5 (gray dashed line), 10 (gray dotted line) and 20 (blue solid line).

(Oelkers et al., 1994), dissolution rates for aluminosilicates – here anorthite and basaltic glass – are controlled by the destruction of silica-rich, Al-deficient surface precursor complexes; a process that is inhibited by free Al^{3+} activity in the fluid. Total Al^{3+} and free Al^{3+} show their highest activities in the M3 model (Fig. 5), thus the Al-inhibition effect is more likely to affect aluminosilicate dissolution rates in this scenario. Aluminosilicate dissolution is enhanced at progressively low pH's in M3, and total Al^{3+} is increased by 4 orders of magnitude allowing free Al^{3+} activity to rise in the fluid by 2 or 3 orders of magnitude. Despite the increase in free Al^{3+}, we found that the effect of the Al-inhibition rate law is indistinguishable from the linear TST-rate simulation; bulk dissolution rates of anorthite and basaltic glass are the same in both cases. Maher et al. (2009) demonstrated that the Al-inhibition formulation results in bigger differences compared to the linear TST law when dissolution is near-equilibrium. Plagioclase and basaltic glass are generally strongly undersaturated during all our simulations with $\log(IAP/K_{eq})$ ranges between < -30 and < 1 (Figures B. 1, B. 4 and B. 5) because of the intensity of the weathering regime with large water/rock ratios and short fluid residence times. Consequently, the Al-inhibition effect on dissolution rates is overpowered by the reaction affinity term (Eq. (2)), with stronger dependence on hydrogen ion activity in the affinity term rather than free Al^{3+} as inhibitor in the rate law.

4.5.2. Acid oxidation mechanism of ferrous Fe

We also tested a different representation of Fe-oxidation that includes acid and neutral mechanisms, according to the rate-law described by Equation (7). The acid mechanism results in overall reduced Fe losses, a shallower reaction front when compared to the original M3, a Fe accumulation layer with positive τ_{Fe} values at the reaction front, and immobility of Fe below the accumulation layer (Fig. 7). This more complex representation of oxidation results on a Fe distribution profile that diverges from the LSAG observations.

The parallel rate-law that includes the acid and neutral oxidation mechanisms results in increased Fe in the column, since it shows faster oxidation rates during the younger stages of weathering (Fig. B.8). These faster reaction rates at the early stages of weathering generate large discrepancies on Fe distribution in the soil column. Considering total Fe^{3+}, free Fe^{3+} activity and precipitated volume of goethite, the parallel-acid oxidation mechanism renders higher values for all three parameters when compared to the neutral-exclusive oxidation mechanism during the first 10 kyr of simulation (Fig. B.9). Differences in total Fe^{3+} and free Fe^{3+} activity are minor ($<$1 order of magnitude) for weathering stages up to 10 kyr, and there are no differences by 20 kyr. Despite these seemingly insignificant differences on dissolved Fe(III), their effect on goethite precipitation is large: predicted goethite volumes at the 20-kyr stage adds up to 3 and 8 % for the neutral-exclusive and parallel-acid oxidation mechanisms respectively. The higher free Fe^{3+} in the parallel-acid oxidation mechanism results in smaller Fe-losses compared to M3 and the LSAG data at 20-kyr because of less dissolution of goethite. The integrated mass transfer values predicted for Fe in the acid oxidation model are 50% lower than the Laupahoehoe data (Table 5). Although M3 (neutral oxidation) overestimates Fe losses and predicts Fe depletion in the first 30 cm of the profile not observed in the data (Fig. 7), the oxidation rates are slower and decrease only by 1–2 orders of magnitude with age; whereas the acid mechanism results in very fast oxidation rates that drastically decrease in time (Fig. B.8), rendering overall less Fe losses than in Laupahoehoe. Ultimately, any of the modeled Fe-oxidation mechanisms here can be interpreted as different representations of the timing and onset of Fe-oxidation in natural systems: (1) the neutral rate as a slow and sustained Fe oxidation that slowly consumes oxygen; or (2) the acid-neutral parallel rate as a fast and efficient oxidation utilizing O_2 rapidly and that declines as Fe-oxyhydroxides coatings cover the primary mineral surfaces.

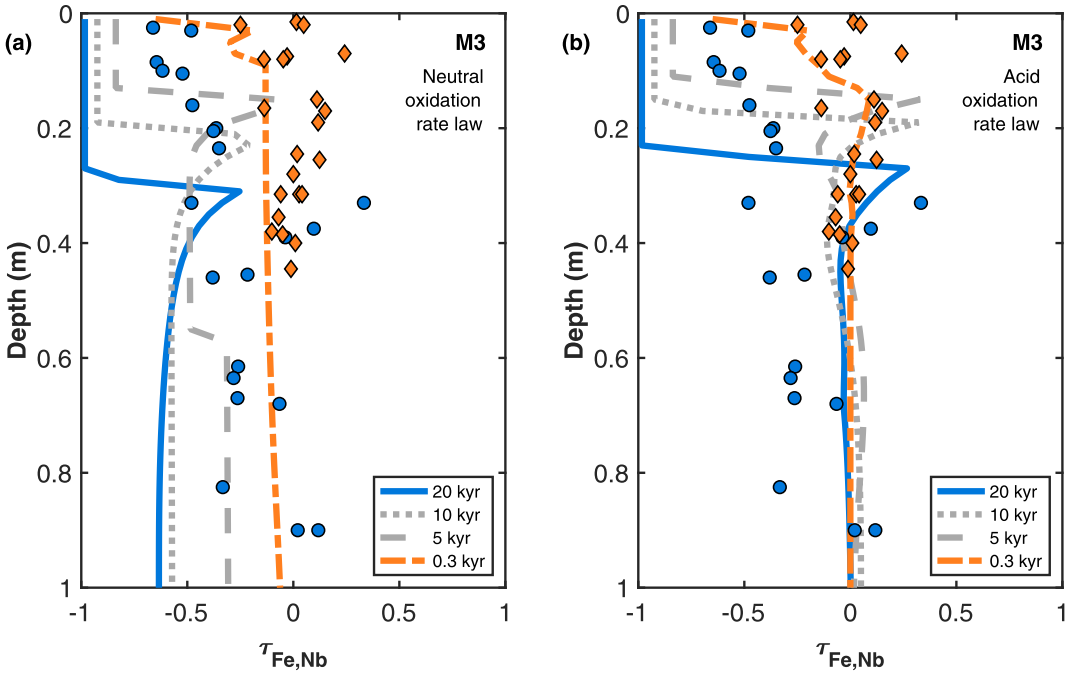

Fig. 7. Comparison of Fe mass distribution ($\tau_{Fe,Nb}$) profiles under two Fe-oxidation mechanisms in the M3 model. Panel (a) shows the neutral-exclusive oxidation rate law. Panel (b) shows the parallel acid-neutral oxidation rate law. Legend and symbols are identical to previous figures.

5. DISCUSSIONS

5.1. Considerations for RTM of basalt weathering

In this series of simulations, we have attempted to test some of the factors contributing to intense weathering of basalts in the Island of Hawai'i. The results from the M3 model provide insight into the processes governing extensive element leaching and mineralogical changes on geologically short timescales. Nevertheless, we did not intend to create a replica of field conditions, and therefore, our simulations are limited in several aspects.

A major caveat of our model is how fluid transport is represented here in comparison to a natural system, as a 1-D steady-state flow cannot represent spatial or temporal heterogeneity in sub-surface flow. In real systems, fluid residence times are heterogeneous since inputs vary with time (Heidbuchel et al., 2012; Harman, 2015) and can influence the shape and depth of weathering fronts (Maher et al., 2009; Maher, 2010). For example, unsteady fluid residence times can shift atmospheric gases contents in the soil leading to soil redox oscillations that potentially increase Fe(III)-oxide crystallinity (Thompson et al., 2006), and change surface properties of minerals (Chorover et al., 2004). The scale of fluid residence time also exerts a primary control on mineral weathering rates. Longer timescales result in slower reaction rates, controlling the extent of weathering fronts. Variable fluid residence time is also a consequence of heterogeneous flow paths. Preferential flow structures allow rapid fluid flow, implying faster weathering rates on these surfaces, while matrix areas experience prolonged contact with fluid and consequently reduced dissolution rates. Despite these obvious differences in fluid transport between our simulations and natural systems, the weathering model here produces a realistic representation of element distribution over 20 kyr, providing a useful tool to understand processes controlling intense weathering of basalts.

Variations in the relative abundance of primary minerals and glass can produce different solute concentrations in the fluid. Here we impose a specific primary mineralogy and no attempts were made to evaluate different mineral

Table 5
Integrated mass transfer coefficients for Si, Ca, Mg, Al and Fe in all three models at 20-kyr, plus the acid Fe oxidation simulation compared to the integrated mass-transfer coefficients in the Laupahoehoe 20 kyr site (in bold).

	M1	M2	M3	M3 + acid oxidation	LSAG
τ_{Si}	−0.67	−0.78	−0.87	−0.88	**−0.91**
τ_{Ca}	−0.89	−0.98	−0.98	−0.98	**−0.95**
τ_{Mg}	−0.54	−0.96	−0.96	−0.97	**−0.92**
τ_{Al}	−0.17	−0.01	−0.47	−0.51	**−0.66**
τ_{Fe}	−0.28	−0.63	−0.69	−0.25	**−0.51**

assemblages. Mineral volume changes in Fig. B.6 are merely illustrative of the underlying processes driving dissolution or precipitation of a phase rather than being a detailed account of mineral distributions in the soil at progressive weathering stages. However, we can use mineral saturation indexes to infer how primary minerals ratios alter fluid chemistry: in our models the larger proportions of highly soluble basaltic glass and plagioclase will increase $SiO_{2(aq)}$ and dissolved Al solute export and enhance total volumetric losses. On the other hand, pyroxene and olivine weather more slowly (despite their slightly faster rate weathering rate constants compared to plagioclase) and increasing their volumetric contents will produce less $SiO2_{(aq)}$ in the fluid when compared to their more soluble counterparts. Another potential mass loss term that we have not attempted to quantify is colloid export, which can impact Al, Si and Fe, and HFSE export from igneous rocks (Bern et al., 2011; Trostle et al., 2016; Aguirre et al., 2017). Colloid export may account for some of the discrepancies between observed and modeled Fe, Si and Al distributions at the 20 kyr site. While it is likely that colloid redistribution plays some role in the evolution of Hawaiian soils the RTM is not well suited to address that specific process.

5.2. Key factors controlling intense basalt weathering

Results from our simulations suggest that biological activity plays a key role enhancing weathering and pedogenesis of basaltic rocks. The role of plants and microbiota accelerating weathering rates in the Earth's surface has been discussed by many authors (Berner, 1997; Drever and Stillings, 1997; Berner and Cochran, 1998; Jones, 1998; Kelly et al., 1998; Moulton and Berner, 1998; Neaman et al., 2005b; Lawrence et al., 2014;). Here we have tried to improve the understanding of how LMWOA and high soil CO_2 enhance chemical weathering rates. As a primary conclusion, it is clear from our results that increasing carbonic and carboxylic acids lower pH in the soil and that pH is a fundamental variable controlling intense weathering. However, a deeper understanding of the role of organic acids in fast chemical weathering requires analysis of modeled solute concentrations and mineral weathering profiles (volume % and saturation state) to understand and quantify their effect in mineral dissolution.

5.2.1. Soil respiration effects on weathering fronts

Carbon dioxide from soil respiration can be several orders of magnitude larger than atmospheric CO_2, and in tropical soils its concentration increases with depth (Fig. A. 1). The organic matter pool constitutes a constant acidity source during pedogenesis and is key to overcoming buffering from dissolution of primary minerals. Because of the CO_2 limitation in the base simulation (M1), pH is very high ($pH > 9$) inhibiting dissolution of magnetite and to a lesser extent pyroxene and olivine. Goethite precipitation is very restricted, because it only reaches supersaturation when enough Fe is available as magnetite is dissolved, rendering integrated Fe losses at 20-kyr that only add up to 28% (Table 5). High CO_2 produced by soil respiration is required to decrease pH in the soil column and trigger dissolution of primary Fe-bearing minerals. Soil respiration in the model (M2) generates sufficient CO_2 to trigger dissolution of ferrous silicates and magnetite. The magnetite weathering front in model M2 moves much faster than the base model (M1), and it disappears from the profile at 20 kyr as magnetite becomes undersaturated at all depths (Fig. B.1). Because dissolution of goethite mostly follows the magnetite weathering front, it becomes slightly supersaturated only when magnetite starts to dissolve. Soil respiration enhances dissolution of all primary Fe-bearing phases, allowing more precipitation of Fe-oxyhydroxides such as goethite.

As discussed before, pH in the base simulation (M1) is rapidly buffered to basic pH values, limiting leaching of elements from some mineral phases. At this high pH range the dissolved activities of $SiO_{2(aq)}$ and free Al^{3+} are minor compared to model M2 (Fig. B.10). Thus, a major consequence of including a soil respiration mechanism in our simulation is increasing dissolved contents of leached cations and silica in the fluid. (Fig. B.10). Free Al^{3+} in the base simulation is low, because at these high pH's Al is dominantly in the form of AlO_2^- and $Al(OH)_4^-$ (Fig. B.2). This results in undersaturation of allophane and imogolite below the topmost portion of the profile (Fig. B.1). Al depletion occurring at these high pH's is a consequence of the low free Al^{3+} activity which controls the affinity term on secondary aluminosilicate precipitation. We can compare these results with the M2 simulation with increased CO_2. Here, allophane and imogolite are always supersaturated (Fig. B.4), since the activities of $SiO_{2(aq)}$ and free Al^{3+} are much higher than the base model, despite lower total Al in the fluid. Here, the fluid stays far-from-equilibrium and supersaturated with respect to the secondary aluminosilicates, allowing imogolite and allophane to precipitate at relatively fast rates.

5.2.2. Organic ligand effects on elemental losses and low pH

Our simulations show that LMW organic acids are key factors contributing to the rapid weathering of basalts in Hawai'i. The simulations describe an intense weathering regime with short fluid residence times that overall results in dissolution of the basaltic parent material. Nevertheless, addition of organic acids in the profile does yield faster dissolution rates for the primary minerals, and importantly hinders precipitation of secondary phases. The inputs of LMWOA to the soil profile generate increasingly acid conditions that affect the affinity term that controls reaction rates of all minerals including weathering products precipitated at earlier weathering stages, while complexation of commonly immobile elements Al and Fe(III) allows continuous leaching of metals from primary and secondary minerals in the weathering rock and soil column.

5.2.2.1. Complexation of Al and Fe drive dissolution of secondary phases. Oxalate and citrate in our final model (M3) generate the conditions necessary to reach the mass loss distributions observed in the LSAG, especially after 20 kyr of continuous high intensity weathering (Fig. 4). Incorporating LWM organic acids to this weathering

scheme not only enhances dissolution of primary phases, but also produces dissolution of precipitated secondary phases and inhibition of precipitation at depth (Figures B. 5 and B. 6). The results from M3 indicate that by 20 kyr all secondary minerals become undersaturated (log $IAP/K_{eq} < 0$) along the profile which results in negative reaction rates and dissolution of allophane, imogolite and goethite. The affinity term controlling the sign and magnitude of the overall reaction rate has a cubic dependence on pH, a linear dependence on Al^{3+} activity and a square-root dependence on $SiO_{2(aq)}$ for imogolite and 0.66 power dependence for allophane (Table 2). The *IAP* for goethite has also a cubic dependence on H^+ and a linear dependence on free Fe^{3+}. To disentangle the effect of each species on the mineral saturation index of secondary phases, we can examine free element activity as a function of *IAP*. As an example, Fig. 8a shows that at 20 kyr the fluid is always undersaturated with respect to allophane, and it only comes close to saturation when the activity of H^+ is lower while Al^{3+} stays relatively low (similar behavior for imogolite). This simple analysis can indicate that the departure from equilibrium for the secondary aluminosilicates is strongly influenced by the low pH provided by the organic acids. The effect of LMWOA in enhancing dissolution of secondary minerals could be just via increased a_{H+}, but also via complexation and a consequent decrease in a_{Al3+} and a_{Fe3+}. If the increased acidity is the main driver, the depletion patterns observed at the 20-kyr site could be generated by inorganic sources of acidity where complex formation is not favorable. To test this idea, we ran a simulation in which oxalate and citrate were present – thus generating acidity – but Al and/or Fe^{3+} were not allowed to form complexes with either ligand. The results show that the organic acids drive dissolution of secondary minerals because they are sources of acidity and because of Al (and Fe(III)) complexation with LMWOA. When complexation of Al is not allowed in the model, the fluid is much closer to saturation with respect to allophane because free Al^{3+} activity is several orders of magnitude higher while $SiO_{2(aq)}$ and pH stay relatively constant (Fig. 8 and 9a). This mechanism prevents dissolution of allophane because dissolution rates slow down when closer to equilibrium (Fig. 9b). In fact, when complexation is suppressed, modeled fluid saturation with respect to allophane is much closer to M2 in which pH is circumneutral, suggesting the importance of Al-organic complex formation in dissolution of secondary minerals (Fig. 9). These results are analogous to modeled *IAP* for imogolite and goethite. At the pH's reached by 20 kyr, in the absence of complexation most of the dissolved Al is in the form of free Al^{3+} instead of being hydrolyzed or complexed (Fig. 9). Complexation of Al with LMWOA lowers the activity of free Al^{3+} by 5–6 orders of magnitude, which significantly impacts the affinity term controlling reaction rates. Therefore, organic acids are not only important as a source of acidity, but also for their role decreasing the activity of free Al^{3+} and Fe^{3+} in the fluid via complex formation. This mechanism appears to be key to explain the large Al (and Si) losses observed in the Hawaiian soils after 20 kyr. It is important to note that the dissolution of secondary minerals when LWMOA are present results from a different mechanism than in the base simulation (M1); where allophane and imogolite are initially supersaturated but then begin to dissolve because of extremely low $SiO_{2(aq)}$ and free Al^{3+} activities at pH values above 8.

5.2.2.2. Implications of LMWOA on interpretation of paleosol data. Given the important effect that LMWOA have in mobilization of Al and Fe(III) from soils, it may be possible to use the behavior of Al in ancient soils as an indicator of the presence of significant terrestrial biomass in the absence of better paleobotanical or paleontological evidences. As demonstrated here, Al depletion requires the presence of organic acids even in a relatively high rainfall regime, and high P_{CO2} alone does not result in Al loss. Fe-depletion patterns can also respond to the presence of subaerial biomass, either by complexation with organic ligands of Fe^{3+} and/or by reductive dissolution in oxygen depleted or/and water-logged conditions (Beukes et al., 2002; Holland and Rye, 1997; Neaman et al., 2005a; Ohmoto, 1996). We therefore propose that Al and Fe depletion patterns in paleosols may be evidence of the presence of a terrestrial biomass capable of generating soil organic matter.

5.3. Discrepancies between distribution of Fe in the model and the LSAG data

As noted in the results section, large discrepancies arise between the modeled total Fe distribution in the profile at 20 kyr with respect to the Laupahoehoe data (Fig. 4c). These discrepancies are the result of the reacting fluid becoming unsaturated with respect to goethite very quickly as a result of low activity of free Fe^{3+} in the model, because most of the dissolved ferric iron is complexed with citrate and oxalate at low pH's. This is confirmed after running M3 without allowing Fe^{3+} to form complexes with citrate and oxalate, in the same fashion as the analyses for role of free Al^{3+} in preventing dissolution of imogolite and allophane. In this case, the fluid approaches equilibrium with respect to goethite by 20 kyr (Fig. B.12). When Fe(III)-complexes are suppressed, the Fe distribution in the profile is constant and equal to Fe losses for model M2 (Fig. 3 and B.13). However, this approach fails to show the enriched Fe layer that is observed at Laupahoehoe and in the complexation model. Given the results from all these simulations, it seems implausible that Fe-oxyhydroxides such as goethite (or ferrihydrite) are the only mineral sink for Fe in these soils, meaning that iron is been retained by processes not described in our model. Fe can be stabilized by interactions with organic matter (Chen et al., 2014; Mikutta et al., 2014), plus 'new' Fe can be added to organic horizons by litter turnover. However, we question whether these mechanisms can account for more than 10% retention of Fe along the entire 1-meter profile as these processes are restricted to O-horizons. Alternatively, Fe can be retained by refractory spinel phases that incorporate Fe(III) in their structure as part of the solid-solution series between brookite (TiO_2 phases found in laterites) and hematite or maghemite (Fe_2O_3), most typically as pseudobrookite ($Fe(III)_2TiO_5$) which is known to occur in Hawaiian soils

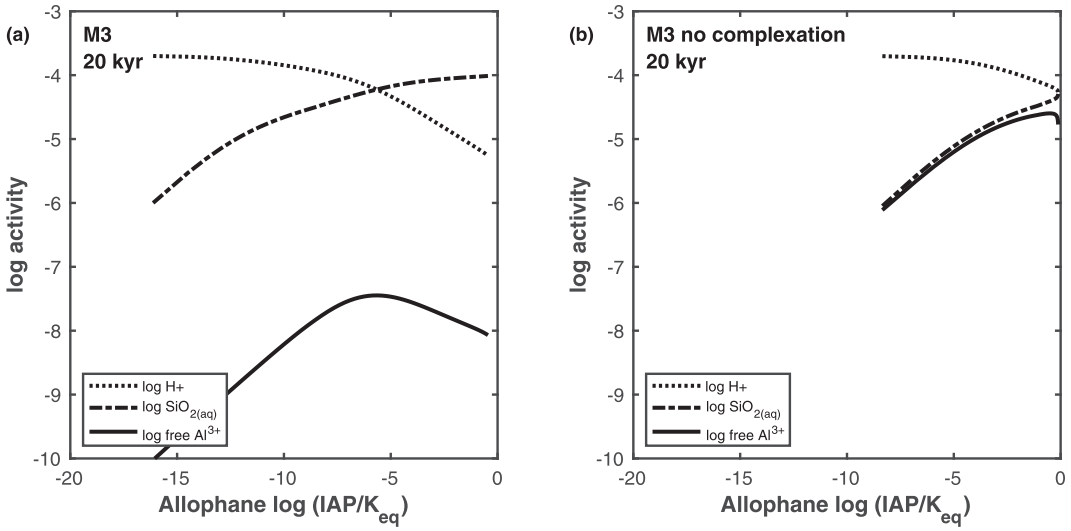

Fig. 8. Activity of H^+ (dotted line), dissolved Al^{3+} (solid line) and $SiO_{2(aq)}$ (dot-dashed line) as a function of Allophane saturation index for model M3 at 20 kyr. (a) shows the results for M3 with Al-LMWOA complex formation. (b) shows M3 with no complexation with LMWOA. In panel (a) the fluid is only close to saturation with respect to allophane when the activity of dissolved silica is high, but it never reaches $IAP/K_{eq} = 1$. When complex formation is suppressed from the model, free Al^{3+} is 5 to 6 orders of magnitude higher and the fluid becomes closer to saturation despite slight decreases in $SiO_{2(aq)}$ and pH. Comparing both results it is clear that complexation generates lower IAP and the system is further from equilibrium.

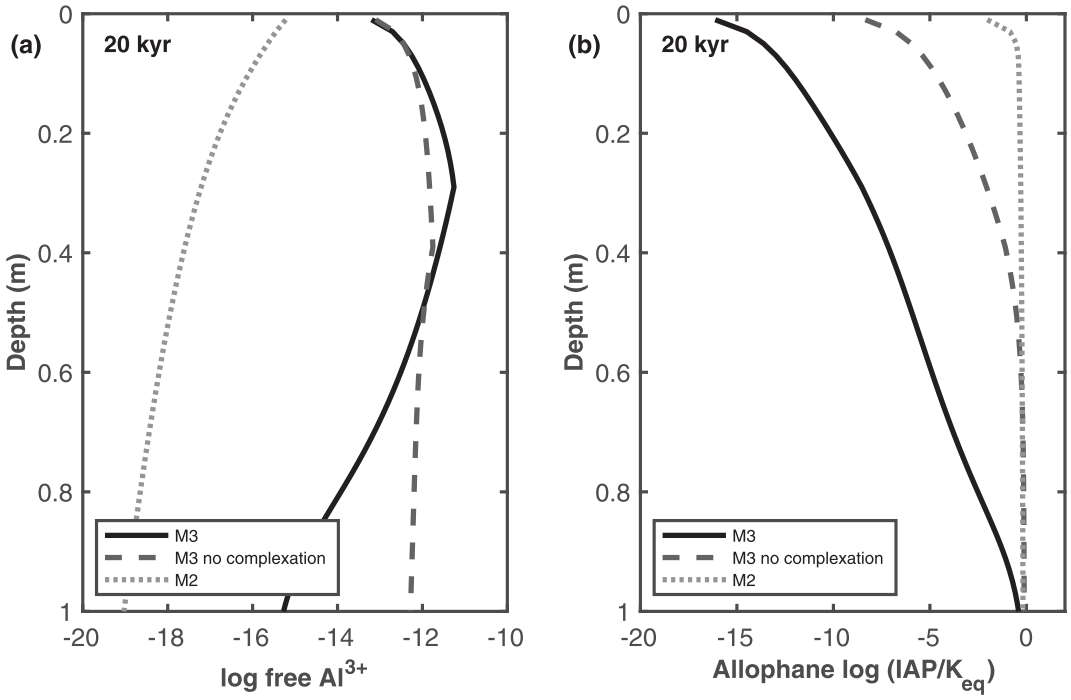

Fig. 9. The effect of addition of organic ligands and complexation on (a) free Al^{3+} activity and (b) allophane saturation index at 20 kyr as a function of depth. Solid-line represents the results for M3 allowing complexation of Al with organic ligands. Dashed line shows M3 without complexation of Al with organic ligands. Dotted line shows the results for M2 with no organic ligands and no complexation. LMWOA complexation of Al lowers the activity of free Al^{3+} by 5–6 orders of magnitude despite high total Al concentration and results in undersaturation with respect to secondary Al phases allophane (shown here) and imogolite. This mechanism appears central to the large aluminum losses observed in highly weathered Hawaiian soils.

(Katsura et al., 1962; Kurtz, 2000; Pett-Ridge et al., 2007; Sherman, 1952; Walker et al., 1969). Titanium in Hawaiian soils is present in primary ilmenite and anatase and is recycled into secondary pseudobrookite and/or brookite during weathering, possibly incorporating Fe(III) into these more refractory phases. Although some degree of Ti mobility

has been observed in the Hawaiian soils (Correns, 1978; Kurtz et al., 2000), Fe/Ti ratios in the most weathered horizons at Laupahoehoe approach the Fe/Ti ratio of pseudobrookite, suggesting that some Fe is ultimately retained in this mineral. In our simulations we did not include Ti-bearing phases because of the lack of thermodynamic data available for Ti-organic complexes to model titanium dissolution and re-precipitation.

5.4. Importance of mineral solubilities for reactive transport modeling

Thermodynamic saturation of primary and secondary minerals controls dissolution rates and propagation of mineral weathering fronts, as changes in the saturation indexes of mineral phases respond to changes in the fluid chemistry (Hellmann and Tisserand, 2006). The reactive transport models of basalt weathering based on the LSAG chronosequence emphasize the importance of this relationship. During the construction of our models, we used different published thermodynamic data to represent the primary and secondary minerals in basalt. Discrepancies between databases result in different solubilities for the same mineral phase, and therefore, it was necessary to carefully evaluate which mineral phases interpreted the elemental distribution coefficients observed in the Hawaiian sites (Kurtz et al., 2000; Vitousek, 2004). This approach is similar to that of Maher et al. (2009) where the solubility of kaolinite was modeled to interpret the mineral distribution in the soil profile. In our simulations we did not attempt to calculate solubility coefficients for any of the minerals involved, because the mineralogy of these soils is not well constrained. However, we did employ this criterion when selecting the mineral phases for our model when large discrepancies between the elemental data and the model arose in the initial runs of the model.

The equilibrium constants determined for the Icelandic Stapafell basaltic glass composition (Aradottir et al., 2012b) have been successfully used during reactive transport modeling of CO_2 sequestration by basaltic minerals (Aradottir et al., 2012a). Initially this basaltic glass was selected, but dissolution occurred much faster compared to our model since log $(IAP/K_{eq}) < -100$. As a result, Si was leached from the system much more rapidly than observations in the LSAG sites. A more reasonable approach was to calculate the equilibrium constant for a Hawaiian basalt, in this case BHVO-2, which rendered a solubility that appeared much more consistent with the Hawai'i soil data. Likewise, the some of the different plagioclase solubilities calculated by Stefansson (2001) are several orders of magnitude larger than those calculated for either anorthite and albite in SUPCRT92, because they considered a higher entropy model. Subsequently, choosing any of the values calculated for the Icelandic basalt resulted in a crystalline phase that was even more soluble than BHVO-2 basaltic glass. The use of primary phase data that is more soluble than our simulations would accentuate the conclusion that affinity is a strong control on basalt weathering rate but would render in faster elemental exports.

The stability and reaction rates of secondary minerals are critical to understanding the extreme elemental mass losses observed in these Hawaiian soils, particularly for Al, Si and Fe. This means that appropriate equilibrium constants for secondary minerals in the model are also critical to characterize these losses. Ferrihydrite is often assumed to be the major Fe weathering product in early-stage development of these Hawaiian soils (Chorover et al., 2004), hence we initially chose ferrihydrite ($Fe(OH)_3$) as the iron sink for our simulations. However, the ion activity product for ferrihydrite decreases rapidly to values lower than the equilibrium constants reported for this phase (Aradottir et al., 2012b; Wolery et al., 1990), resulting in faster Fe losses in the weathering column than observed in the Hawaiian sites. Consequently, a less soluble phase was required as the ferric iron precipitate for this model. This indirect result is fully consistent with a Mössbauer spectroscopy study of Fe in similar Hawaiian soils (Thompson et al. (2006). They found that the SRO-mineral fraction in young-intermediate age soils contained nano-goethite and nano-hematite rather than a non-crystalline, ferrihydrite-like precursor. We found that by specifying goethite as the secondary Fe sink (in place of ferrihydrite) the agreement between the model and observed soil distributions of Fe improved.

6. CONCLUSIONS

The models developed in this study establish key factors controlling intensively weathering patterns in Hawaiian basalts. High soil CO_2 and organic acids contribute to already reactive conditions with short-fluid residence times and hydrological unsaturation in the bedrock/soil. This work emphasizes the role of soil Pco_2 and low molecular weight organic acids in sustaining far-from-equilibrium conditions that result in fast propagation of reaction fronts and ultimately generate element depletion patterns in this system.

The reactive transport simulations of a chronosequence of basaltic soils in the Island of Hawai'i were generated using the reactive transport code CrunchFlow. The modeling approach was to reproduce pH and the mass-depletion profiles of Ca, Mg, Si, Al and Fe. Starting with an infiltrating fluid just in equilibrium with atmospheric CO_2, we then sequentially incorporated: (1) soil respiration by a constant CO_2 flux that keeps up with infiltration and reaction rates and rising P_{CO2} by one order of magnitude from atmospheric; and (2) organic acids by adding 100 μM of oxalate and citrate to the reacting fluid and allowing these to form complexes with Al and Fe(III). Decomposition of the organic molecules contributed negligibly to increased soil CO_2 in the model. Our results indicate that elevated and constant CO_2 inputs from soil respiration supply necessary acidity to remove base cations (Ca^{2+}, Mg^{2+}) from the system, and buffer fluid and soil pH to circumneutral values after 20,000 years. At these neutral pH's secondary minerals accumulate and prevent leaching of Si and refractory Fe(III) and Al. Incorporation of LMW organic ligands, in this case oxalate and citrate, is necessary to achieve the patterns of low pH's and Si, Fe and Al mass depletion observed in these Hawaiian soils. At the low pH values both observed and modeled for the highly weathered soil

suppression or dissolution of secondary minerals permits Al, Si and Fe leaching from the upper region of the weathering profile. Dissolution of secondary minerals is driven by activity of H^+ and complexation of Al and Fe(III) with organic ligands enhances this effect by reducing the activities of Al^{3+} and Fe^{3+} in the fluids at low pH's. Our model results imply that oxalate is more efficient for Al mobilization whereas citrate is more effective for leaching Fe(III). Additionally, we tested an Al-inhibition rate-law for dissolution of basaltic glass and plagioclase and the incorporation of the acid oxidation mechanism of ferrous to ferric iron. The Al-inhibition formulation was no different to the results obtained from the linear TST approach. The results showcase that at far-from-equilibrium conditions the inhibition effect of free Al^{3+} in the rate law is not important since dissolution is driven by the affinity term. The importance of affinity is likely to be a general result for weathering of intermediate and basic volcanic products, as the primary phases in these rocks are typically strongly undersaturated under a wide range of natural water compositions (Ibarra et al., 2016). This implies that uncertainties in kinetic rate constants should not substantially hinder the application of RTMs to this genre of problem. When comparing the acid and neutral oxidation rate law for iron, the acid mechanism results in faster and greater concentration of Fe(III) in the fluid, allowing more Fe-oxide precipitation and less export of iron from the soil profile. Overall our results point towards the importance of consistent far-from-equilibrium conditions to produce intensively weathered soils developed from basaltic lava flows.

This work adds to previous contributions on reactive transport models of weathering, by understanding processes controlling weathering of basaltic rocks at shorter geological timescales (10^3 – 10^4 years). This model can be extrapolated to weathering in other tropical or high primary productivity regions dominated by mafic and intermediate lithologies, to recognize governing factors driving mineral dissolution and precipitation and metal/nutrient losses.

ACKNOWLEDGEMENTS

We are grateful to Kate Maher (Stanford University) for providing training and assistance using CrunchFlow in 2016. We would like to thank Oliver Chadwick (University of California, Santa Barbara) for providing chemical data from the LSAG, and Katherine Bland for field support and data analysis with soil pH, moisture and CO_2 measurements. A.P acknowledges CONICYT PFCHA/Doctorado Becas Chile/2014 - 72150180 and the Fulbright International Student Program for PhD fellowships. This study was partially supported by NSF 1349269 to L. Derry and Integral Fellowship awards to A. Perez-Fodich. We are thankful for the detailed and thoughtful reviews by the Associate Editor Chen Zhu and reviewers, which greatly improved the quality of this paper.

APPENDIX A. SOIL CARBON FLUXES AND PRODUCTION

Soil CO_2 efflux from the surface is the respiration of roots and decomposition of organic matter. Measurements soil pH and soil moisture (Fig. A.1) and of soil CO_2 efflux (Fig. A.2) from the soil were carried out by L.A. Derry and students in EAS 3220 over four years from 2010 to 2013 on the SW flank of Kohala volcano in the Island of Hawai'i (Bland et al., 2013). While the substrate age there is older (350 kyr) than the sites used in this study, soil chemistry is similar to the 20 kyr Laupahoehoe site. Sites were selected to represent different rainfall regimes (positively correlated with elevation) and different vegetation between forest and pasture sites. Multiple cycles of CO_2 influx rate were measured with a LiCOR 6400 flux analyzer to calculate the soil CO_2 flux. Each measurement was calculated

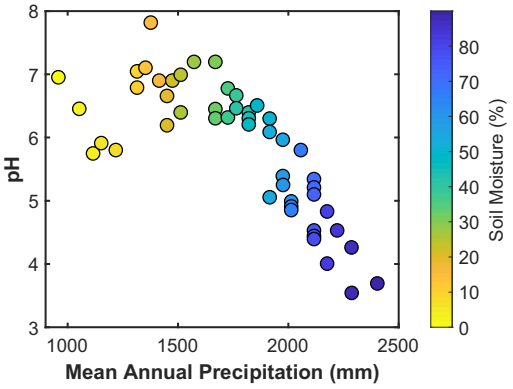

Fig. A.1. Summary of soil pH and soil moisture (%) as a function of mean annual precipitation (mm) in a climate gradient in the Island of Hawai'i. Circles indicate soil pH, and color bar shows the moisture content of the soil. (For interpretation of the color legend, the reader is referred to the online version of this article).

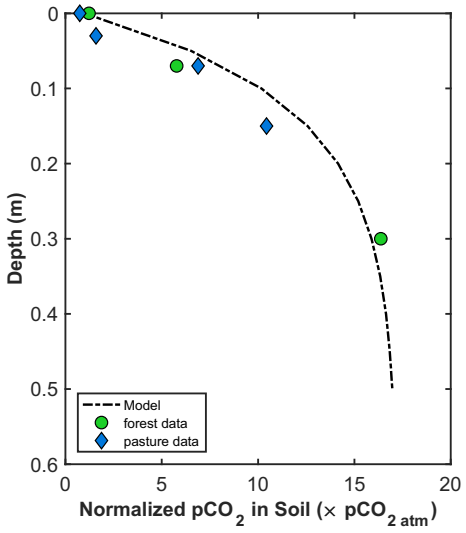

Fig. A.2. CO_2 concentration measured in two types of Hawaiian soils (pasture and forest) and reaction-diffusion CO_2 model. Forest data is represented by green circles and pasture data by blue diamonds. Modeled CO_2 fugacity (dot-dashed line) is calculated using average measured CO_2 surface efflux of 8μmol m^{-2} s^{-1}, diffusivity coefficient D=0.04 cm^2 s^{-1}, and atmospheric $P_{CO2} = 380$ ppmv.

from the average of 5 cycles of measured CO_2 efflux at each of 3 separate locations on a 5 m equilateral triangle. The CO_2 average fluxes were: mesic pasture 8.5 μmol m^{-2} s^{-1}, mesic forest 6.3 μmol m^{-2} s^{-1}, lowland dry grassland 1.2 μmol m^{-2} s^{-1} and lowland dry forest 7.3 μmol m^{-2} s^{-1}.

A reaction-diffusion model can represent the soil CO_2 concentration profile with depth. Conservation of mass requires that the output CO_2 flux is equal to the input flux plus the production term $R_{co2}(z)$. CO_2 production was modeled as an exponential function of depth:

$$R_{CO_2}(z) = R_0 e^{-z/h} \tag{A.1}$$

where $R_{co2}(z)$ is CO_2 production per unit volume, R_0 is the scaled surface flux scaled, h is the scale length and z is depth. Diffusion of CO_2 controls the transfer of carbon dioxide between the soil and the atmosphere and within soil layers. Assuming a no-flux boundary condition from the bottom of the soil profile, we can integrate the CO_2 flux as a function of depth as:

$$F(z) = R_0 h e^{-z/h} \tag{A.2}$$

Thus, we can retrieve the surface flux F_{surf} as:

$$F_{surf} = R_o h \tag{A.3}$$

Integrating the production term R_{CO2}, and using the atmospheric boundary condition $C_0 = 390$ ppmv, plus the diffusion coefficient in the soil $D = 4 \times 10^{-6}$ (m^2 s^{-1}), we can obtain an expression to model the soil CO_2 concentration as a function of depth:

$$C(z) = C_0 + \frac{F_{surf} h}{D}(1 - e^{-z/h}) \tag{A.4}$$

Using Eq. (A.4), we estimate the CO_2 concentration as a function of depth in a 60-cm soil profile, which is shown in Fig. A.2. Soil CO_2 concentrations increase with depth as it is diffused downwards the soil profile from an organic rich layer. The production of CO_2 is modeled using Eq. (A.1) and decreases with depth as there is only a surface organic reservoir.

APPENDIX B. SUPPLEMENTARY MATERIAL

Supplementary data to this article can be found online at https://doi.org/10.1016/j.gca.2019.01.027.

REFERENCES

Aagaard P. and Helgeson H. C. (1982) Thermodynamic and kinetic constraints on reaction-rates among minerals and aqueous-solutions. 1. Theoretical considerations. *Am. J. Sci.* **282**, 237–285.

Advocat, T., Chouchan, J.L., Crovisier, J.L., Guy, C., Daux, V., Jegou, C., Gin, S., Vernaz, E., 1997. Borosilicate nuclear waste glass alteration kinetics: chemical inhibition and affinity control. In: 21st International Symposium on the Scientific Basis for Nuclear Waste Management, Davos, Switzerland. pp. 63–70.

Aguirre A. A., Derry L. A., Mills T. J. and Anderson S. P. (2017) Colloidal transport in the Gordon Gulch catchment of the Boulder Creek CZO and its effect on C-Q relationships for silicon. *Water Resour. Res.* **53**, 2368–2383.

Amrhein C. and Suarez D. L. (1988) The use of a surface complexation model to describe the kinetics of ligand-promoted dissolution of anorthite. *Geochim. Cosmochim. Acta* **52**, 2785–2793.

Amundson R., Richter D. D., Humphreys G. S., Jobbagy E. G. and Gaillardet J. (2007) Coupling between biota and earth materials in the Critical Zone. *Elements* **3**, 327–332.

Aoki M., Fujii K. and Kitayama K. (2012) Environmental control of root exudation of low-molecular weight organic acids in tropical rainforests. *Ecosystems* **15**, 1194–1203.

Aradottir E. S. P., Sonnenthal E. L., Bjornsson G. and Jonsson H. (2012a) Multidimensional reactive transport modeling of CO_2 mineral sequestration in basalts at the Hellisheidi geothermal field, Iceland. *Int. J. Greenhouse Gas Control* **9**, 24–40.

Aradottir E. S. P., Sonnenthal E. L. and Jonsson H. (2012b) Development and evaluation of a thermodynamic dataset for phases of interest in CO_2 mineral sequestration in basaltic rocks. *Chem. Geol.* **304**, 26–38.

Bacon D. H. and Keller C. K. (1998) Carbon dioxide respiration in the deep vadose zone: Implications for groundwater age dating. *Water Resour. Res.* **34**, 3069–3077.

Barman A. K., Varadachari C. and Ghosh K. (1992) Weathering of silicate minerals by organic-acids. 1. Nature of cation solubilization. *Geoderma* **53**, 45–63.

Engott, J.A., 2011. A water-budget model and assessment of groundwater recharge for the Island of Hawai'i., Scientific Investigations Report. U. S. Geological Survey, p. 53.

Becker J. J., Sandwell D. T., Smith W. H. F., Braud J., Binder B., Depner J., Fabre D., Factor J., Ingalls S., Kim S. H., Ladner R., Marks K., Nelson S., Pharaoh A., Trimmer R., Von Rosenberg J., Wallace G. and Weatherall P. (2009) Global bathymetry and elevation data at 30 arc seconds resolution: SRTM30_PLUS. *Mar. Geod.* **32**, 355–371.

Berggren D. and Mulder J. (1995) The role of organic-matter in controlling aluminum solubility in acidic mineral soil horizons. *Geochim. Cosmochim. Acta* **59**, 4167–4180.

Bern C. R., Chadwick O. A., Hartshorn A. S., Khomo L. M. and Chorover J. (2011) A mass-balance model to separate and quantify colloidal and solute redistributions in soil. *Chem. Geol.* **282**, 113–119.

Berner R. A. (1992) Weathering, plants, and the long-term carbon-cycle. *Geochim. Cosmochim. Acta* **56**, 3225–3231.

Berner R. A. (1997) Paleoclimate - The rise of plants and their effect on weathering and atmospheric CO2. *Science* **276**, 544–546.

Berner R. A. and Cochran M. F. (1998) Plant-induced weathering of Hawaiian basalts. *J. Sediment. Res.* **68**, 723–726.

Berner R. A., Lasaga A. C. and Garrels R. M. (1983) The carbonate-silicate geochemical cycle and its effect on atmospheric carbon-dioxide over the past 100 million years. *Am. J. Sci.* **283**, 641–683.

Beukes N. J., Dorland H., Gutzmer J., Nedachi M. and Ohmoto H. (2002) Tropical laterites, life on land, and the history of atmospheric oxygen in the Paleoproterozoic. *Geology* **30**, 491–494.

Bland, K., Bitan, K., Finneran, B., Kirk, K., Reed, E., Walsh, M., Winkler, V., Derry, L.A., Moore, A., 2013. The relationship between carbon fluxes, precipitation, and soil properties along a climate gradient, Kohala Volcano, Hawai'i, GSA Annual Meeting. Geological Society of America, Denver, CO.

Bluth G. J. S. and Kump L. R. (1994) Lithologic and climatologic controls of river chemistry. *Geochim. Cosmochim. Acta* **58**, 2341–2359.

Bourcier, W.L., Weed, H.C., Nguyen, S.N., Nielsen, J.K., Morgan, L., Newton, L., Knauss, K.G., 1992. Solution compositional effects on the dissolution kinetics of borosilicate glass.

Brantley S. L. (2005) Reaction kinetics of primary rock-forming minerals under ambient conditions. *Surface Ground Water Weather. Soils* **5**, 73–117.

Brantley S. L. and Lebedeva M. (2011) Learning to read the chemistry of regolith to understand the critical zone. *Annu. Rev. Earth Planet. Sci.* **39**, 387–416.

Brimhall G. H. and Dietrich W. E. (1987) Constitutive mass balance relations between chemical-composition, volume, density, porosity and strain in metasomatic hydrochemical systems – results on weathering and pedogenesis. *Geochim. Cosmochim. Acta* **51**, 567–587.

Brounce M., Stolper E. and Eiler J. (2017) Redox variations in Mauna Kea lavas, the oxygen fugacity of the Hawaiian plume, and the role of volcanic gases in Earth's oxygenation. *Proc. Natl. Acad. Sci. USA* **114**, 8997–9002.

Buss H. L., Mathur R., White A. F. and Brantley S. L. (2010) Phosphorus and iron cycling in deep saprolite, Luquillo Mountains, Puerto Rico. *Chem. Geol.* **269**, 52–61.

Cama J. and Ganor J. (2006) The effects of organic acids on the dissolution of silicate minerals: a case study of oxalate catalysis of kaolinite dissolution. *Geochim. Cosmochim. Acta* **70**, 2191–2209.

Chadwick O. A., Brimhall G. H. and Hendricks D. M. (1990) From a black to a gray box-a mass balance interpretation of pedogenesis. *Geomorphology* **3**, 369–390.

Chadwick O. A., Derry L. A., Vitousek P. M., Huebert B. J. and Hedin L. O. (1999) Changing sources of nutrients during four million years of ecosystem development. *Nature* **397**, 491–497.

Chadwick O. A., Gavenda R. T., Kelly E. F., Ziegler K., Olson C. G., Elliott W. C. and Hendricks D. M. (2003) The impact of climate on the biogeochemical functioning of volcanic soils. *Chem. Geol.* **202**, 195–223.

Chen C. M., Dynes J. J., Wang J. and Sparks D. L. (2014) Properties of Fe-organic matter associations via coprecipitation versus adsorption. *Environ. Sci. Technol.* **48**, 13751–13759.

Chorover J., Amistadi M. K. and Chadwick O. A. (2004) Surface charge evolution of mineral-organic complexes during pedogenesis in Hawaiian basalt. *Geochim. Cosmochim. Acta* **68**, 4859–4876.

Correns C. W. (1978) Titanium. In *Handbook of Geochemistry* (ed. K. H. Wedepohl). Springer-Verlag, Berlin.

Crews T. E., Kitayama K., Fownes J. H., Riley R. H., Herbert D. A., Muellerdombois D. and Vitousek P. M. (1995) Changes in soil-phosphorus fractions and ecosystems dynamics across a long chronosequence in Hawaii. *Ecology* **76**, 1407–1424.

Delany, J.M., Wolery, T.J., 1989. The LLNL thermochemical database. Report UCRL-21658.

Dessert C., Dupre B., Francois L. M., Schott J., Gaillardet J., Chakrapani G. and Bajpai S. (2001) Erosion of Deccan Traps determined by river geochemistry: impact on the global climate and the Sr-87/Sr-86 ratio of seawater. *Earth Planet. Sci. Lett.* **188**, 459–474.

Dessert C., Lajeunesse E., Lloret E., Clergue C., Crispi O., Gorge C. and Quidelleur X. (2015) Controls on chemical weathering on a mountainous volcanic tropical island: Guadeloupe (French West Indies). *Geochim. Cosmochim. Acta* **171**, 216–237.

Dontsova K., Steefel C. I., Desilets S., Thompson A. and Chorover J. (2009) Solid phase evolution in the Biosphere 2 hillslope experiment as predicted by modeling of hydrologic and geochemical fluxes. *Hydrol. Earth Syst. Sci.* **13**, 2273–2286.

Drever J. I. and Stillings L. L. (1997) The role of organic acids in mineral weathering. *Colloids Surfaces a-Physicochem. Eng. Aspects* **120**, 167–181.

Engott, J.A., 2011. A water-budget model and assessment of groundwater recharge for the Island of Hawai'i, Scientific Investigations Report. U. S. Geological Survey. p. 53.

Fox T. R. and Comerford N. B. (1990) Low-molecular-weight organic-acids in selected forest soils of the southeastern usa. *Soil Sci. Soc. Am. J.* **54**, 1139–1144.

Fujii K., Aoki M. and Kitayama K. (2012) Biodegradation of low molecular weight organic acids in rhizosphere soils from a tropical montane rain forest. *Soil Biol. Biochem.* **47**, 142–148.

Furrer G. and Stumm W. (1986) The coordination chemistry of weathering.1. Dissolution kinetics of delta-Al_2O_3 and BeO. *Geochim. Cosmochim. Acta* **50**, 1847–1860.

Gaillardet J., Dupre B., Louvat P. and Allegre C. J. (1999) Global silicate weathering and CO_2 consumption rates deduced from the chemistry of large rivers. *Chem. Geol.* **159**, 3–30.

Ganor J., Lu P., Zheng Z. P. and Zhu C. (2007) Bridging the gap between laboratory measurements and field estimations of silicate weathering using simple calculations. *Environ. Geol.* **53**, 599–610.

Ganor J., Reznik I. J. and Rosenberg Y. O. (2009) Organics in water-rock interactions. *Thermodyn. Kinetics Water-Rock Interact.* **70**, 259–369.

Giambelluca T. W., Chen Q., Frazier A. G., Price J. P., Chen Y. L., Chu P. S., Eischeid J. K. and Delparte D. M. (2013) Online rainfall atlas of Hawai'i. *Bull. Amer. Meteorol. Soc.* **94**, 313–316.

Gislason S. R., Arnorsson S. and Armannsson H. (1996) Chemical weathering of basalt in southwest Iceland: effects of runoff, age of rocks and vegetative/glacial cover. *Am. J. Sci.* **296**, 837–907.

Gislason S. R. and Oelkers E. H. (2003) Mechanism, rates, and consequences of basaltic glass dissolution: II. An experimental study of the dissolution rates of basaltic glass as a function of pH and temperature. *Geochim. Cosmochim. Acta* **67**, 3817–3832.

Godderis Y., Brantley S. L., Francois L. M., Schott J., Pollard D., Deque M. and Dury M. (2013) Rates of consumption of atmospheric CO_2 through the weathering of loess during the next 100 yr of climate change. *Biogeosciences* **10**, 135–148.

Gruber C., Harpaz L., Zhu C., Bullen T. D. and Ganor J. (2013) A new approach for measuring dissolution rates of silicate minerals by using silicon isotopes. *Geochim. Cosmochim. Acta* **104**, 261–280.

Harman C. J. (2015) Time-variable transit time distributions and transport: Theory and application to storage-dependent transport of chloride in a watershed. *Water Resour. Res.* **51**, 1–30.

He Y., Li D. C., Velde B., Yang Y. F., Huang C. M., Gong Z. T. and Zhang G. L. (2008) Clay minerals in a soil chronosequence derived from basalt on Hainan Island, China and its implication for pedogenesis. *Geoderma* **148**, 206–212.

Hedin L. O., Vitousek P. M. and Matson P. A. (2003) Nutrient losses over four million years of tropical forest development. *Ecology* **84**, 2231–2255.

Heidbuchel I., Troch P. A., Lyon S. W. and Weiler M. (2012) The master transit time distribution of variable flow systems. *Water Resour. Res.* **48**, 19.

Helgeson H. C. (1969) Thermodynamics of hydrothermal systems at elevated temperatures and pressures. *Am. J. Sci.* **267**, 729-&.

Helgeson H. C., Delany J. M., Nesbitt H. W. and Bird D. K. (1978) Summary and critique of the thermodynamic properties of rock-forming minerals. *Am. J. Sci.* **278**, 1–229.

Helgeson H. C. and Kirkham D. H. (1974a) Theoretical prediction of thermodynamic behavior of aqueous electrolytes at high pressures and temperatures.1. Summary of thermodynamic-electrostatic properties of solvent. *Am. J. Sci.* **274**, 1089-&.

Helgeson H. C. and Kirkham D. H. (1974b) Theoretical prediction of thermodynamic behavior of aqueous electrolytes at high pressures and temperatures. 2. Debye-huckel parameters for activity-coefficients and relative partial molal properties. *Am. J. Sci.* **274**, 1199-&.

Helgeson H. C., Kirkham D. H. and Flowers G. C. (1981) Theoretical prediction of the thermodynamic behavior of aqueous-electrolytes at high-pressures and temperatures. 4. Calculation of activity-coefficients, osmotic coefficients, and apparent molal and standard and relative partial molal properties to 600-degrees-C and 5 kb. *Am. J. Sci.* **281**, 1249–1516.

Hellmann R. and Tisserand D. (2006) Dissolution kinetics as a function of the Gibbs free energy of reaction: an experimental study based on albite feldspar. *Geochim. Cosmochim. Acta* **70**, 364–383.

Helz R. T., Cottrell E., Brounce M. N. and Kelley K. A. (2017) Olivine-melt relationships and syneruptive redox variations in the 1959 eruption of Kilauea Volcano as revealed by XANES. *J. Volcanol. Geotherm. Res.* **333**, 1–14.

Holland H. D. and Rye R. (1997) Evidence in pre-2.2 Ga paleosols for the early evolution of atmospheric oxygen and terrestrial biota: comment. *Geology* **25**, 857–858.

Ibarra D. E., Caves J. K., Moon S., Thomas D. L., Hartmann J., Chamberlain C. P. and Maher K. (2016) Differential weathering of basaltic and granitic catchments from concentration-discharge relationships. *Geochim. Cosmochim. Acta* **190**, 265–293.

Johnson J. W., Oelkers E. H. and Helgeson H. C. (1992) SUPCRT92 – A software package for calculating the standard molal thermodynamic properties of minerals, gases, aqueous species, and reactions from 1-bar to 5000-bar and 0-degrees-C to 1000-degrees-C. *Comput. Geosci.* **18**, 899–947.

Johnson S. B., Yoon T. H., Slowey A. J. and Brown G. E. (2004) Adsorption of organic matter at mineral/water interfaces: 3. Implications of surface dissolution for adsorption of oxalate. *Langmuir* **20**, 11480–11492.

Jones D. L. (1998) Organic acids in the rhizosphere – a critical review. *Plant Soil* **205**, 25–44.

Jones D. L. and Darrah P. R. (1994) Role of root derived organic-acids in the mobilization of nutrients from the rhizosphere. *Plant Soil* **166**, 247–257.

Katsura T., Kushiro I., Akimoto S.-I., Walker J. L. and Sherman G. D. (1962) Titanomagnetite and titanomaghemite in a Hawaiian soil. *J. Sediment. Res.* **32**, 299–308.

Keller C. K. and Wood B. D. (1993) Possibility of chemical-weathering before the advent of vascular land plants. *Nature* **364**, 223–225.

Kelly E. F., Chadwick O. A. and Hilinski T. E. (1998) The effect of plants on mineral weathering. *Biogeochemistry* **42**, 21–53.

Kitayama K., Muellerdombois D. and Vitousek P. M. (1995) Primary succession of Hawaiian montane rain-forest on a chronosequence of 8 lava flows. *J. Veg. Sci.* **6**, 211–222.

Kump L. R., Brantley S. L. and Arthur M. A. (2000) Chemical, weathering, atmospheric CO_2, and climate. *Annu. Rev. Earth Planet. Sci.* **28**, 611–667.

Kurtz A. C. (2000) *Germanium/Silicon and Trace Elemental Geochemistry of Silicate Weathering and Mineral Aerosol Deposition*. Cornell University, Ithaca, NY.

Kurtz A. C., Derry L. A. and Chadwick O. A. (2001) Accretion of Asian dust to Hawaiian soils: isotopic, elemental, and mineral mass balances. *Geochim. Cosmochim. Acta* **65**, 1971–1983.

Kurtz A. C., Derry L. A., Chadwick O. A. and Alfano M. J. (2000) Refractory element mobility in volcanic soils. *Geology* **28**, 683–686.

Lasaga, A.C., 1981. Rate laws of chemical reactions. In: Lasaga, A. C., Kirkpatrick, R.J. (Eds.), Kinetics of Geochemical Processes. Mineralogical Society of America, Reviews in Mineralogy. pp. 1–67.

Lasaga A. C. (1984) Chemical-kinetics of water-rock interactions. *J. Geophys. Res.* **89**, 4009–4025.

Lau L. S. and Mink J. F. (2006) *Hydrology of the Hawaiian Islands*. University of Hawai'i Press, Honolulu.

Lawrence C., Harden J. and Maher K. (2014) Modeling the influence of organic acids on soil weathering. *Geochim. Cosmochim. Acta* **139**, 487–507.

Leturcq G., Berger G., Advocat T. and Vernaz E. (1999) Initial and long-term dissolution rates of aluminosilicate glasses enriched with Ti, Zr and Nd. *Chem. Geol.* **160**, 39–62.

Li G. J., Hartmann J., Derry L. A., West A. J., You C. F., Long X. Y., Zhan T., Li L. F., Li G., Qiu W. H., Li T., Liu L. W., Chen Y., Ji J. F., Zhao L. and Chen J. (2016) Temperature dependence of basalt weathering. *Earth Planet. Sci. Lett.* **443**, 59–69.

Li J., Xu R., Tiwari D. and Ji G. (2006) Effect of low-molecular-weight organic acids on the distribution of mobilized Al between soil solution and solid phase. *Appl. Geochem.* **21**, 1750–1759.

Li L., Maher K., Navarre-Sitchler A., Druhan J., Meile C., Lawrence C., Moore J., Perdrial J., Sullivan P., Thompson A., Jin L. X., Bolton E. W., Brantley S. L., Dietrich W. E., Mayer K. U., Steefel C. I., Valocchi A., Zachara J., Kocar B., McIntosh J., Tutolo B. M., Kumar M., Sonnenthal E., Bao C. and Beisman J. (2017) Expanding the role of reactive transport models in critical zone processes. *Earth Sci. Rev.* **165**, 280–301.

Lohse K. A. and Dietrich W. E. (2005) Contrasting effects of soil development on hydrological properties and flow paths. *Water Resour. Res.* **41**, W12419–W12419.

Louvat P. and Allegre C. J. (1997) Present denudation rates on the island of Reunion determined by river geochemistry: basalt weathering and mass budget between chemical and mechanical erosions. *Geochim. Cosmochim. Acta* **61**, 3645–3669.

Macdonald, G.A., Abbott, A.T., Peterson, F.L., 1984. Volcanoes in the Sea: The Geology of Hawaii, second ed.

Maher K. (2010) The dependence of chemical weathering rates on fluid residence time. *Earth Planet. Sci. Lett.* **294**, 101–110.

Maher K., Steefel C. I., White A. F. and Stonestrom D. A. (2009) The role of reaction affinity and secondary minerals in regulating chemical weathering rates at the Santa Cruz Soil Chronosequence, California. *Geochim. Cosmochim. Acta* **73**, 2804–2831.

Marin-Spiotta E., Chadwick O. A., Kramer M. and Carbone M. S. (2011) Carbon delivery to deep mineral horizons in Hawaiian rain forest soils. *J. Geophys. Res.-Biogeosci.* **116**, 14.

Mikutta R., Lorenz D., Guggenberger G., Haumaier L. and Freund A. (2014) Properties and reactivity of Fe-organic matter associations formed by coprecipitation versus adsorption: clues from arsenate batch adsorption. *Geochim. Cosmochim. Acta* **144**, 258–276.

Moore J., Lichtner P. C., White A. F. and Brantley S. L. (2012) Using a reactive transport model to elucidate differences between laboratory and field dissolution rates in regolith. *Geochim. Cosmochim. Acta* **93**, 235–261.

Morrey, J.R., Krupka, K.M., Dove, F.H., 1985. MINTEQ2 geochemical code: provisionary organic data base, United States, p. 61.

Moulton K. L. and Berner R. A. (1998) Quantification of the effect of plants on weathering: studies in Iceland. *Geology* **26**, 895–898.

Moulton K. L., West A. J. and Berner R. A. (2000) Solute flux and mineral mass balance approaches to the quantification of plant effects on silicate weathering. *Am. J. Sci.* **300**, 539–570.

Moussallam Y., Oppenheimer C., Scaillet B., Gaillard F., Kyle P., Peters N., Hartley M., Berlo K. and Donovan A. (2014) Tracking the changing oxidation state of Erebus magmas, from mantle to surface, driven by magma ascent and degassing. *Earth Planet. Sci. Lett.* **393**, 200–209.

NADP/NTN, D., 2017. National Atmospheric Deposition Program (NRSP-3). NADP Program Office, Illinois State Water Survey, 2204 Griffith Dr., Champaign, IL 61820.

Navarre-Sitchler A., Steefel C. I., Sak P. B. and Brantley S. L. (2011) A reactive-transport model for weathering rind formation on basalt. *Geochim. Cosmochim. Acta* **75**, 7644–7667.

Neaman A., Chorover J. and Brantley S. L. (2005a) Element mobility patterns record organic ligands in soils on early Earth. *Geology* **33**, 117–120.

Neaman A., Chorover J. and Brantley S. L. (2005b) Implications of the evolution of organic acid moieties for basalt weathering over geological time. *Am. J. Sci.* **305**, 147–185.

Neaman A., Chorover J. and Brantley S. L. (2006) Effects of organic ligands on granite dissolution in batch experiments at pH 6. *Am. J. Sci.* **306**, 451–473.

Nieuwenhuyse A., Verburg P. S. J. and Jongmans A. G. (2000) Mineralogy of a soil chronosequence on andesitic lava in humid tropical Costa Rica. *Geoderma* **98**, 61–82.

Oelkers E. H., Benezeth P. and Pokrovski G. S. (2009) Thermodynamic databases for water-rock interaction. *Thermodyn. Kinet. Water-Rock Interact.* **70**, 1–46.

Oelkers E. H. and Gislason S. R. (2001) The mechanism, rates and consequences of basaltic glass dissolution: I. An experimental study of the dissolution rates of basaltic glass as a function of aqueous Al, Si and oxalic acid concentration at 25 degrees C and pH=3 and 11. *Geochim. Cosmochim. Acta* **65**, 3671–3681.

Oelkers E. H. and Schott J. (1998) Does organic acid adsorption affect alkali-feldspar dissolution rates? *Chem. Geol.* **151**, 235–245.

Oelkers E. H., Schott J. and Devidal J. L. (1994) The effect of aluminum, pH, and chemical affinity on the rates of aluminosilicate dissolution reactions. *Geochim. Cosmochim. Acta* **58**, 2011–2024.

Ohmoto H. (1996) Evidence in pre-2.2 Ga paleosols for the early evolution of atmospheric oxygen and terrestrial biota. *Geology* **24**, 1135–1138.

Olsen A. A. and Rimstidt J. D. (2008) Oxalate-promoted forsterite dissolution at low pH. *Geochim. Cosmochim. Acta* **72**, 1758–1766.

Palandri, J., Kharaka, Y., 2004. A compilation of rate parameters of water-mineral interaction kinetics for application to geochemical modeling., U.S. Geological Survey Open File Report 204-1068. U.S. Geological Survey. p. 64.

Paul A. (1977) Chemical durability of glasses – thermodynamic approach. *J. Mater. Sci.* **12**, 2246–2268.

Pett-Ridge J. C., Monastra V. M., Derry L. A. and Chadwick O. A. (2007) Importance of atmospheric inputs and Fe-oxides in controlling soil uranium budgets and behavior along a Hawaiian chronosequence. *Chem. Geol.* **244**, 691–707.

Pokrovskii V. A. and Helgeson H. C. (1995) Thermodynamic properties of aqueous species and the solubilities of minerals at high pressures and temperatures: the system Al2O3-H2O-NaCl. *Am. J. Sci.* **295**, 1255–1342.

Pokrovskii V. A. and Helgeson H. C. (1997) Thermodynamic properties of aqueous species and the solubilities of minerals at high pressures and temperatures: the system Al2O3-H2O-KOH. *Chem. Geol.* **137**, 221–242.

Pokrovsky O. S. and Schott J. (2000) Kinetics and mechanism of forsterite dissolution at 25 degrees C and pH from 1 to 12. *Geochim. Cosmochim. Acta* **64**, 3313–3325.

Prapaipong P., Shock E. L. and Koretsky C. M. (1999) Metal-organic complexes in geochemical processes: temperature dependence of the standard thermodynamic properties of aqueous complexes between metal cations and dicarboxylate ligands. *Geochim. Cosmochim. Acta* **63**, 2547–2577.

Rimstidt J. D. and Barnes H. L. (1980) The kinetics of silica-water reactions. *Geochim. Cosmochim. Acta* **44**, 1683–1699.

Ruan H. D. and Gilkes R. J. (1995) Acid dissolution of synthetic aluminous goethite before and after transformation to hematite by heating. *Clay Miner.* **30**, 55–65.

Saar M. O. and Manga M. (1999) Permeability-porosity relationship in vesicular basalts. *Geophys. Res. Lett.* **26**, 111–114.

Schopka H. H. and Derry L. A. (2012) Chemical weathering fluxes from volcanic islands and the importance of groundwater: the Hawaiian example. *Earth Planet. Sci. Lett.* **339**, 67–78.

Schopka H. H., Derry L. A. and Arcilla C. A. (2011) Chemical weathering, river geochemistry and atmospheric carbon fluxes from volcanic and ultramafic regions on Luzon Island, the Philippines. *Geochim. Cosmochim. Acta* **75**, 978–1002.

Schott J., Berner R. A. and Sjoberg E. L. (1981) Mechanism of pyroxene and amphibole weathering.1. Experimental studies of iron-free minerals. *Geochim. Cosmochim. Acta* **45**, 2123–2135.

Schwartzman D. W. (2017) Life's critical role in the long-term carbon cycle: the biotic enhancement of weathering. *AIMS Geosci.* **3**, 216–238.

Schwartzman D. W. and Volk T. (1989) Biotic enhancement of weathering and the habitability of Earth. *Nature* **340**, 457–460.

Sherman G. D. (1952) The titanium content of hawaiian soils and its significance. *Soil Sci. Soc. Am. Proc.* **16**, 15–18.

Shock E. L. and Helgeson H. C. (1988) Calculation of the thermodynamic and transport-properties of aqueous species at high-pressures and temperatures – correlation algorithms for ionic species and equation of state predictions to 5-kb and 1000-degrees-C. *Geochim. Cosmochim. Acta* **52**, 2009–2036.

Shock E. L. and Koretsky C. M. (1993) Metal-organic complexes in geochemical processes – calculation of standard partial molal thermodynamic properties of aqueous acetate complexes at high-pressures and temperatures. *Geochim. Cosmochim. Acta* **57**, 4899–4922.

Shock E. L., Sassani D. C., Willis M. and Sverjensky D. A. (1997) Inorganic species in geologic fluids: correlations among standard molal thermodynamic properties of aqueous ions and hydroxide complexes. *Geochim. Cosmochim. Acta* **61**, 907–950.

Singer P. C. and Stumm W. (1970) Acidic mine drainage – Rate-determining step. *Science* **167**, 1121-&.

Sposito, G., Mattigold, S.V., 1980. GEOCHEM - A computer program for the calculation of chemical equilibria in soil solutions and other natural water systems, Riverside, CA.

Steefel C. I., Appelo C. A. J., Arora B., Jacques D., Kalbacher T., Kolditz O., Lagneau V., Lichtner P. C., Mayer K. U., Meeussen J. C. L., Molins S., Moulton D., Shao H., Simunek J., Spycher N., Yabusaki S. B. and Yeh G. T. (2015) Reactive transport codes for subsurface environmental simulation. *Comput. Geosci.* **19**, 445–478.

Stefansson A. (2001) Dissolution of primary minerals of basalt in natural waters – I. Calculation of mineral solubilities from 0 degrees C to 350 degrees C. *Chem. Geol.* **172**, 225–250.

Stefansson A. and Gislason S. R. (2001) Chemical weathering of basalts, Southwest Iceland: effect of rock crystallinity and secondary minerals on chemical fluxes to the ocean. *Am. J. Sci.* **301**, 513–556.

Stewart B. W., Capo R. C. and Chadwick O. A. (1998) Quantitative strontium isotope models for weathering, pedogenesis and biogeochemical cycling. *Geoderma* **82**, 173–195.

Stillings L. L., Drever J. I. and Poulson S. R. (1998) Oxalate adsorption at a plagioclase (An(47)) surface and models for ligand-promoted dissolution. *Environ. Sci. Technol.* **32**, 2856–2864.

Strom L., Olsson T. and Tyler G. (1994) Differences between calcifuge and acidifuge plants in root exudation of low-molecuiar organic-acids. *Plant Soil* **167**, 239–245.

Sverdrup H. and Warfvinge P. (1988) Weathering of primary silicate minerals in the natural soil environment in relation to a chemical-weathering model. *Water Air Soil Pollut.* **38**, 387–408.

Sverjensky D. A., Shock E. L. and Helgeson H. C. (1997) Prediction of the thermodynamic properties of aqueous metal complexes to 1000 degrees C and 5 kb. *Geochim. Cosmochim. Acta* **61**, 1359–1412.

Taylor L. L., Leake J. R., Quirk J., Hardy K., Banwart S. A. and Beerling D. J. (2009) Biological weathering and the long-term carbon cycle: integrating mycorrhizal evolution and function into the current paradigm. *Geobiology* **7**, 171–191.

Techer I., Advocat T., Lancelot J. and Liotard J. M. (2001) Dissolution kinetics of basaltic glasses: control by solution chemistry and protective effect of the alteration film. *Chem. Geol.* **176**, 235–263.

Thompson A., Chadwick O. A., Rancourt D. G. and Chorover J. (2006) Iron-oxide crystallinity increases during soil redox oscillations. *Geochim. Cosmochim. Acta* **70**, 1710–1727.

Torn M. S., Trumbore S. E., Chadwick O. A., Vitousek P. M. and Hendricks D. M. (1997) Mineral control of soil organic carbon storage and turnover. *Nature* **389**, 170–173.

Trostle K. D., Runyon J. R., Pohlmann M. A., Redfield S. E., Pelletier J., McIntosh J. and Chorover J. (2016) Colloids and organic matter complexation control trace metal concentration-discharge relationships in Marshall Gulch stream waters. *Water Resour. Res.* **52**, 7931–7944.

van Hees P. A. W., Jones D. L., Finlay R., Godbold D. L. and Lundstomd U. S. (2005) The carbon we do not see - the impact of low molecular weight compounds on carbon dynamics and respiration in forest soils: a review. *Soil Biol. Biochem.* **37**, 1–13.

van Hees P. A. W., Lundstrom U. S. and Giesler R. (2000) Low molecular weight organic acids and their Al-complexes in soil solution - composition, distribution and seasonal variation in three podzolized soils. *Geoderma* **94**, 173–200.

van Hees P. A. W., Vinogradoff S. I., Edwards A. C., Godbold D. L. and Jones D. L. (2003) Low molecular weight organic acid adsorption in forest soils: effects on soil solution concentrations and biodegradation rates. *Soil Biol. Biochem.* **35**, 1015–1026.

Viers J., Dupre B. and Gaillardet J. (2009) Chemical composition of suspended sediments in World Rivers: New insights from a new database. *Sci. Total Environ.* **407**, 853–868.

Vitousek, P., 2004. Nutrient cycling and limitation: Hawai'i as a model system. Nutrient cycling and limitation: Hawai'i as a model system., i-xx, 1-223.

Vitousek P. M., Chadwick O. A., Crews T., Heath J., Hedin L. O., Kurtz A. and Matson P. A. (2001) Element inputs and outputs across a substrate age gradient in the Hawaiian Islands. *Ecol. Soc. Am. Ann. Meet. Abstracts* **86**, 226-226.

Vitousek P. M., Chadwick O. A., Crews T. E., Fownes J. H., Hendricks D. M. and Herbert D. A. (1997) Soil and ecosystem development across the Hawaiian islands. *GSA Today* **7**, 1–8.

Walker J. C. G., Hays P. B. and Kasting J. F. (1981) A negative feedback mechanism for the long-term stabilization of Earths surface-temperature. *J. Geophys. Res.-Oceans* **86**, 9776–9782.

Walker J. L., Sherman G. D. and Katsura T. (1969) Iron and titanium minerals in titaniferous ferruginous latosols of Hawaii. *Pac. Sci.* **23**, 291-&.

Welch S. A. and Ullman W. J. (2000) The temperature dependence of bytownite feldspar dissolution in neutral aqueous solutions of inorganic and organic ligands at low temperature (5–35 degrees C). *Chem. Geol.* **167**, 337–354.

Wessel P., Smith W. H. F., Scharroo R., Luis J. and Wobbe F. (2013) Generic mapping tools: improved version released. *EOS, Trans. Am. Geophys. Union* **94**, 409–410.

White A. F., Blum A. E., Schulz M. S., Bullen T. D., Harden J. W. and Peterson M. L. (1996) Chemical weathering rates of a soil chronosequence on granitic alluvium. 1. Quantification of mineralogical and surface area changes and calculation of primary silicate reaction rates. *Geochim. Cosmochim. Acta* **60**, 2533–2550.

White A. F. and Brantley S. L. (2003) The effect of time on the weathering of silicate minerals: why do weathering rates differ in the laboratory and field? *Chem. Geol.* **202**, 479–506.

White A. F., Peterson M. L. and Hochella M. F. (1994) Electrochemistry and dissolution kinetics of magnetite and ilmenite. *Geochim. Cosmochim. Acta* **58**, 1859–1875.

White A. F., Schulz M. S., Stonestrom D. A., Vivit D. V., Fitzpatrick J., Bullen T. D., Maher K. and Blum A. E. (2009) Chemical weathering of a marine terrace chronosequence, Santa Cruz, California. Part II: Solute profiles, gradients and the comparisons of contemporary and long-term weathering rates. *Geochim. Cosmochim. Acta* **73**, 2769–2803.

Wilson, S.A., 1997. Data compilationf for USGS reference material BHVO-2, Hawaiian Basalt: USGS Open-File Report xxxxx. U. S. Geological Survey.

Winnick M. J. and Maher K. (2018) Relationships between CO2, thermodynamic limits on silicate weathering, and the strength of the silicate weathering feedback. *Earth Planet. Sci. Lett.* **485**, 111–120.

Wolery, T.J., 1992. EQ3/EQ6, a software package for geochemical modeling of aqueous systems, package overview and installation guide (version 7.0). Report UCRL-MA-110662(1). Lawrence Livermore National Laboratory.

Wolery T. J. and Colon C. F. J. (2017) Chemical thermodynamic data. 1. The concept of links to the chemical elements and the historical development of key thermodynamic data. *Geochim. Cosmochim. Acta* **213**, 635–676.

Wolery T. J., Jackson K. J., Bourcier W. L., Bruton C. J., Viani B. E., Knauss K. G. and Delany J. M. (1990) Current status of the EQ3/6 software package for geochemical modeling. *ACS Symp. Ser.* **416**, 104–116.

Wood B. D., Keller C. K. and Johnstone D. L. (1993) Insitu measurement of microbial activity and controls on microbial CO2 production in the unsaturated zone. *Water Resour. Res.* **29**, 647–659.

Wymore A. S., Brereton R. L., Ibarra D. E., Maher K. and McDowell W. H. (2017) Critical zone structure controls concentration-discharge relationships and solute generation in forested tropical montane watersheds. *Water Resour. Res.* **53**, 6279–6295.

Yang L. and Steefel C. I. (2008) Kaolinite dissolution and precipitation kinetics at 22 degrees C and pH 4. *Geochim. Cosmochim. Acta* **72**, 99–116.

Zehetner F., Miller W. P. and West L. T. (2003) Pedogenesis of volcanic ash soils in Andean Ecuador. *Soil Sci. Soc. Am. J.* **67**, 1797–1809.

Zhu C., Liu Z. Y., Zhang Y. L., Wang C., Scheafer A., Lu P., Zhang G. R., Georg R. B., Yuan H. L. and Rimstidt J. D. (2016) Measuring silicate mineral dissolution rates using Si isotope doping. *Chem. Geol.* **445**, 146–163.

Zimmer K., Zhang Y. L., Lu P., Chen Y. Y., Zhang G. R., Dalkilic M. and Zhu C. (2016) SUPCRTBL: a revised and extended thermodynamic dataset and software package of SUPCRT92. *Comput. Geosci.* **90**, 97–111.

Zinder B., Furrer G. and Stumm W. (1986) The coordination chemistry of weathering. 2. Dissolution of Fe(III) oxides. *Geochim. Cosmochim. Acta* **50**, 1861–1869.

Associate editor: Chen Zhu